Title

Low photorespiratory capacity is sufficient to block the induction of high photosynthetic capacity in high light.

Authors

Christopher R. Baker[1*], Jean Christophe Cocurrun[2], Ana Paula Alonso[2,3], Krishna K. Niyogi[1,4]

[1]Howard Hughes Medical Institute, Dept. of Plant and Microbial Biology, University of California, Berkeley, CA 94720-3102, USA

[2]BioDiscovery Institute, University of North Texas, Denton, TX 76201, USA

[3]Department of Biological Sciences, University of North Texas, Denton, TX 76201, USA

[4]Molecular Biophysics and Integrated Bioimaging Division, Lawrence Berkeley National Laboratory, Berkeley, CA 94720, USA

*Corresponding author: cbaker@berkeley.edu

Abstract

The induction of high photosynthetic capacity in high light (HL) is a common response among many herbaceous dicot plants, however, the signaling and metabolic networks that control this response remain largely unknown. Here, multiple independent lines of evidence are presented in support of the conclusion that strong photosynthetic capacity acclimation in HL in *Arabidopsis thaliana* depends on high photorespiratory capacity. Ecotypic variation in the induction of high photosynthetic capacity following a shift to growth in HL was measured across a large *Arabidopsis thaliana* ecotype panel. Comparative differences in primary nitrogen (N) assimilation, photorespiration, and triose-phosphate utilization pathways during the shift to HL were characterized using metabolomic data collected from a strongly acclimating ecotype and a weakly acclimating ecotype. Informed by the behavior of these ecotypes at the extremes, rates of N assimilation and photorespiration using metabolic indicators for these pathways and enzyme activities for key enzymes in these pathways were measured in the full ecotype panel. N assimilation and photorespiration rates early in the HL shift are shown to positively correlate with the magnitude of induction of photosynthetic capacity later in the HL shift. Weakly acclimating ecotypes and photorespiratory mutants when shifted into HL growth under non-photorespiratory conditions gained the ability to strongly induce high photosynthetic capacity in HL. Thus, a negative photorespiration-dependent signal early in the HL shift appears to block photosynthetic capacity acclimation in ecotypes and mutants with low photorespiratory capacity, whereas ecotypes with high photorespiratory capacity are licensed to increase photosynthetic capacity.

Introduction

Photosynthetic organisms tune photosynthetic capacity (i.e., the CO_2- and light-saturated maximum photosynthetic rate) in response to environmental and developmental signals (Bjorkman & Holmgren, 1963; Evans & Poorter, 2001; Athanasiou *et al.*, 2010; Demmig-Adams *et al.*, 2017). For instance, many herbaceous dicot plants increase photosynthetic capacity in response to growth in high light (HL) relative to growth in low light (LL) (Murchie and Horton, 1997; Björkman, 1981). Increasing photosynthetic capacity in crops has been proposed as a means to increase agricultural yields in this century (Long et al., 2015; Parry et al., 2011; Driever et al., 2014). An understanding of how endogenous signaling and metabolic acclimation responses tune photosynthetic capacity in response to the growth environment will accelerate and support engineering approaches to increase photosynthetic capacity.

The acclimation of photosynthetic capacity to HL is part of the suite of acclimation responses that maintain redox poise of the photosynthetic electron transport (PET) chain in HL (Anderson and Osmond, 1987; Savitch et al., 2000; Park et al., 1996; Demmig-Adams et al., 2017; Herrmann et al., 2019). The PET chain is reduced in HL as excess excitation energy exceeds the capacity of downstream reactions to utilize the end products of PET (Li et al., 2009). q_L, a chlorophyll fluorescence parameter that measures the oxidation state of the photosystem II (PSII) electron acceptor site $Q_{A,}$ can be used to quantify the redox state of the PET chain (Kramer et al., 2004). To increase q_L under HL growth (i.e., to oxidize the PET chain), photosynthetic organisms can decrease light absorption and/or divert a greater fraction of absorbed light energy into non-photochemical energy dissipation mechanisms (Bailey et al., 2001; Anderson et al., 1988; Bailey et al., 2004). Increased utilization of the products of PET can also mitigate end-product inhibition of PET in HL (Hald et al., 2008; Pammenter et al., 1993; Foyer et al., 2003). Finally, increased photosynthetic capacity via greater resource allocation to building the components of PET and the Calvin-Benson-Bassham (CBB) cycle will also increase q_L in HL (Walters et al., 2003; Evans and Poorter, 2001; Björkman, 1981). Thus, the acclimation of photosynthetic capacity in HL can be thought of both as a means to balance photosynthetic energy production with sink utilization and as a photoprotective response necessary in excess light environments.

Photosynthetic capacity can be estimated using three parameters: (1) chlorophyll fluorescence-derived estimation or by using the measurement of CO_2 assimilation rates over a

range of intracellular CO_2 concentrations that covers saturating to CO_2 limiting conditions (an A-*Ci* curve) in order to calculate the light-saturated, maximum electron transport rate (ETR_{max}), (2) the CO_2 and light-saturated, maximum oxygen evolution rate (P_{max}), and (3) the CO- and light-saturated, maximum CO_2 assimilation rate (A_{max}). When performing these measurements in high throughput on plants acclimated to different growth environments, careful consideration needs to be given to measurement regimes in order to achieve accurate estimation of photosynthetic capacity (Loreto et al., 2009; Evans et al., 2017; McClain and Sharkey, 2020; Carrier et al., 1989). For instance, it is typical that HL acclimation induces a considerable reduction in the size of light-harvesting antenna linked to PSII, which, if not considered during the calculation of ETR_{max}, can lead to an overestimation of the increase in photosynthetic capacity in HL-grown leaves relative to LL-grown leaves(Strand, 2014). Thus, multiple, independent methodologies for quantifying photosynthetic capacity are used to strengthen conclusions regarding acclimation to the growth environment(Walters et al., 2003; McClain and Sharkey, 2020).

In dicots, multiple days of growth in HL are required before increased photosynthetic capacity is observed (Athanasiou et al., 2010; Walters et al., 2003). In the model herbaceous dicot *Arabidopsis thaliana*, some ecotypes can respond to a shift into HL with a leaf thickness-independent increase in photosynthetic capacity in four to five days (Athanasiou et al., 2010). That this increased photosynthetic capacity is leaf thickness-independent is important because long-term acclimation to HL for most dicots includes the development of thicker leaves (Björkman, 1981), as a consequence of additional palisade layers and/or longer palisade cells (Hanson, 1917; Evans and Poorter, 2001). Photosynthetic capacity, in plants, is typically expressed on a leaf area basis (m^{-2}), thus the thicker leaves developed in HL have higher photosynthetic capacity than thin leaves developed in LL. Normalization of photosynthetic capacity by dry leaf weight per unit area (DW^{-1}), a value that closely tracks with leaf thickness, can provide an alternative methodology to compare photosynthetic capacity between plants with different leaf thicknesses (Stewart et al., 2017; Givnish, 1988; Evans and Poorter, 2001). Species and ecotypes that exhibit strong acclimation of photosynthetic capacity use both leaf thickness-dependent and leaf thickness-independent (cell biological) mechanisms to increase photosynthetic capacity in HL, a group that includes ecotypes of *A. thaliana* as well as diverse species such as *Atriplex triangularis*, *Urtica dioica*, and *Radyera farragei,* whereas other species

and ecotypes appear to exclusively use leaf thickness-dependent mechanisms to increase photosynthetic capacity in HL (Evans and Poorter, 2001; Murchie and Horton, 1997; Givnish, 1988; Athanasiou et al., 2010). A comparative approach between species and ecotypes with different acclimation responses to HL provides a path towards identifying the signaling pathways and metabolic pathways underlying the cell biological-mediated contributions to increased photosynthetic capacity in HL-grown plants.

The acclimation of photosynthetic capacity to HL depends on a plant's dynamic metabolic response of foliar metabolism plants (Demmig-Adams et al., 2014; Häusler et al., 2014; Herrmann et al., 2019; Ma et al., 2014). In addition to carbon (C) signals, the nitrogen (N) state of the plant is also a key regulatory node controlling the acclimation of photosynthetic capacity to HL (Evans and Poorter, 2001; Paul and Pellny, 2003). Primary nitrogen assimilation is induced in HL as the enhanced PET rate increases the supply of reducing equivalents in the chloroplast (Foyer et al., 2003; Osmond et al., 1997). Nitrogen assimilation depends on the activity of chloroplastic enzymes glutamine synthetase (GS) and glutamine-oxoglutarate glutamate aminotransferase (Fd-GOGAT) (Fig. S1A). Thus, increased nitrogen assimilation rates in HL can be observed as an increase in glutamine (Gln)- and glutamate (Glu)-derived amino acids (AAs), and in particular, as an increase in the Gln/Glu ratio in HL in a manner that is proportional to the rate of PET in HL (Foyer et al., 2003, 1994). Linking C and N metabolism, the maintenance of high N-assimilation rates in HL-grown plants will depend on an enhanced supply of organic acids (OAs) to the chloroplast (Nunes-Nesi et al., 2010; Dutilleul et al., 2005). These OAs can either be supplied via the *de-novo* synthesis of OAs through anaplerotic reactions or the mobilization of existing stores of OAs in leaves (Pracharoenwattana et al., 2010).

Enhanced rates of photorespiration are intertwined with increased primary nitrogen assimilation rates in HL (Rachmilevitch et al., 2004). Photorespiration rates in HL increase as a consequence of high PET and Rubisco carboxylation rates that typically drive down intracellular CO_2 levels without a commensurate decrease in O_2 levels (Ma et al., 2014; Keeley and Rundel, 2003). For example, in *A. thaliana,* acclimation to HL roughly doubled the carboxylation rate, whereas photorespiratory flux increased by ~3.3 times(Ma et al., 2014). Additionally, triose phosphate utilization pathways are often rate-limiting for photosynthesis in HL, and in such circumstances, photorespiration acts as a critical photoprotective pathway and valve to convert excess sugar-phosphates into AAs (Busch et al., 2018; Wingler et al., 2000; Dirks et al., 2012).

In much the same way as Gln/Glu can be used as a proxy for nitrogen assimilation and PET rates, the ratio of glycine (Gly) to serine (Ser) can be used as a metabolic indicator of photorespiration rates (Foyer et al., 2003). 2-phosphoglycolate generated by photorespiration is converted into the Gly in the peroxisome, and then in the mitochondria, glycine decarboxylase (GDC) converts Gly into Ser (Fig. S1B), which is a rate-limiting step for photorespiration under strong photorespiratory conditions (Timm et al., 2012). The GDC reaction also releases NH_4^+ as a byproduct, which is reassimilated predominantly via the chloroplastic GS and Fd-GOGAT enzymes, again highlighting the interconnectedness of the N assimilation and photorespiration pathways(Leegood et al., 1995). Recently it has been shown that photorespiratory metabolic signals may repress photosynthesis, and whether this type of signal might influence the acclimation of photosynthetic capacity to HL is unknown (Li et al., 2019; Flügel et al., 2017).

In this work, the increase in photosynthetic capacity in response to a shift to HL growth is measured in *A. thaliana* using a phenotypically diverse panel of genome-sequenced ecotypes (Cao et al., 2011) and supplemented by a detailed investigation of three well-studied ecotypes adapted to contrasting environmental conditions (Stewart et al., 2017). In order to identify metabolites linked to photosynthetic capacity acclimation, metabolomic data was generated for an ecotype with strong photosynthetic capacity acclimation to HL and a second ecotype with weak acclimation to HL. The relationship of N assimilation and photorespiration rates to the acclimation of photosynthetic capacity to HL was tested by quantifying metabolic indicators of N assimilation (Gln/Glu) and photorespiration (Gly/Ser) for the complete ecotype panel during the shift to HL. Further, ecotypes and mutants in photorespiration were shifted into HL in low O_2 and high O_2 conditions, thereby allowing for quantification of acclimation to photosynthetic capacity in HL environments with modified rates of photorespiration. Our findings demonstrate a positive coupling between indicators of N assimilation and photorespiration rate early in the HL shift, as well as for GS activity, and the magnitude of the increase in photosynthetic capacity later in the HL shift. Multiple, independent lines of evidence converge on the conclusion that high photorespiratory capacity is necessary for the efficient induction of photosynthetic capacity during the HL-shift.

Materials & Methods

Plant material and growth conditions

Arabidopsis thaliana ecotypes Castelnuovo-12 (IT) [ABRC stock number: CS98761], Rodasen-47 (SW) [ABRC stock number: CS98762], Col-0, and a set of 80 genome-sequenced ecotypes(Cao et al., 2011) [ABRC stock number: CS76427] were germinated following a one-week dark-cold treatment on ½ MS plates (Murashige & Skoog with Vitamins, Caisson Labs, Smithfield, UT) at 100 µmol photons m^{-2} s^{-1} in a Percival Scientific E36HID growth chamber (Perry, IA, USA) and transferred to 2.5-inch square pots with a 3.5-inch depth containing Sungro Sunshine Mix 4 (Agawam, MA, USA) 10 days post-germination. For more information on the IT and SW ecotypes, see (Oakley *et al.*, 2014; Stewart *et al.*, 2017). Two lines from the set of 80 ecotypes [ABRC stock number: CS76427] were absent from the collection at the time of this work [Mer6, ABRC stock number: CS76414 & Aitba-2, ABRC stock number: CS76347], and two lines did not have sufficient germination events to obtain an acceptable number of replicates [Castelfeld-4-212, ABRC stock number: CS76355 & Lecho-1, ABRC stock number: CS76731]; consequently, the responses of only 76 of the 80 total ecotypes were determined. Potted seedlings were grown for an additional 4 weeks in a shaded, short-day greenhouse (8-h photoperiod at 20 ℃/17.5 ℃ [light/dark] with supplemental lighting (Lumigrow Pro 325, Emeryville, CA, USA) to maintain a daytime light level between 80 and 120 µmol photons m^{-2} s^{-1}. Six ecotypes that had small rosettes under the pre-HL shift conditions were grown for 10 additional days in order to produce sufficient biomass prior to the HL shift (Bozen-1.2, Leb-3, Kly-1, Shigu-1, Koz-2, Shigu-2). Plants were randomly shuffled each day to prevent positional effects, watered every other day, and fertilized once per week using Professional 20-20-20 (Scotts Company, Marysville, OH, USA). LL-grown and HL-shifted plants were transferred in parallel for 4 days to 100 µmol photons m^{-2} s^{-1} and 800 µmol photons m^{-2} s^{-1} in a Conviron E15 growth chamber (Controlled Environments Ltd., Manitoba, Canada) with the same day-length and ambient temperatures.

Chemicals and reagents

Standards for the metabolomic study were purchased from Sigma (St. Louis, MO, USA). [U-$^{13}C_4$]fumarate, [U-$^{13}C_2$]glycine, and [U-$^{13}C_6$]glucose were purchased from Isotec (Miamisburg, OH, USA). LC-MS grade acetonitrile was purchased from Thermo Fisher

(Pittsburgh, PA, USA). For targeted metabolite and enzymatic assays, Amplex Red was purchased from Thermo Fisher Scientific (Waltham, MA, USA), and all enzymes were purchased from Sigma except glycine (Gly) oxidase, D-serine (Ser) dehydratase, and L-Ser racemase (BioVision, Milipitas, CA, USA).

Leaf phenotypic traits

Photosynthetic electron transport rates were estimated by the equation ETR = ΦPSII x α x β x *I* x γ, where ΦPSII is the operating efficiency of photosystem II (PSII), α is the leaf absorptance value, β is the fraction of light absorbed by PSII, *I* is the photon flux density applied to the sample, and γ is the relative efficiency of light absorption of blue and red light (Loreto et al., 2009; McClain and Sharkey, 2020). The variables β and γ were assumed to be constant across our samples (0.5 and 0.75, respectively) given the identical light quality for the growth regime of all plants and shared light quality and intensity used for all samples in the measurement regime (Mekala et al., 2015). Leaf absorptance (α) was estimated using the empirically derived formula first proposed by Evans(Evans, 1996) as Chl per unit area/(Chl per unit area + 0.076), in which Chl per unit area was expressed in units of mmol m^{-2}. ΦPSII was measured in tandem with q_L, a measure of the oxidation state of the primary electron acceptor of PSII, Q_A, using a pulse-amplitude-modulated (PAM) chlorophyll fluorometer (FMS2; Hansatech Instruments Ltd., Norfolk, UK) as previously described (Brooks and Niyogi, 2011). Briefly, light-acclimated leaves were subjected to 6.5 min of strong, white LED actinic light (1650 µmol photons m^{-2} s^{-1}) and steady-state fluorescence (F_s) levels were recorded. Maximum fluorescence levels (F_m') were obtained by applying a saturating pulse of light (0.8 s of 3000 µmol photons m^{-2} s^{-1}) at 3 min, 5 min, and 6.5 min, and minimum fluorescence levels (F_o') were recorded by briefly darkening the leaf, followed by a short far-red light pulse. Q_A reduction state was calculated as $1 - q_L = (1/F_s - 1/F_m')/(1/F_o' - 1/F_m')$. ΦPSII was calculated as ΦPSII = $(F_m' - F_s)/F_m'$. Maximum O_2 evolution rates were determined as light- and CO_2-saturated O_2 evolution with leaf-disc O_2 electrodes (Hansatech Instruments Ltd., Norfolk, UK) as previously described(Delieu and Walker, 1981). Gas exchange measurements were performed using the LI-COR 6400XT (LI-COR, Lincoln, NE) as previously described (Long and Bernacchi, 2003; Sharkey, 1988). Saturating light levels, as well as saturating CO_2 levels, were empirically determined using the SW ecotype prior to commencing this work (Fig. S1). Chlorophyll (Chl) *a*

& *b* content per unit area was determined via spectrophotometry as previously described (Ritchie, 2006, 2008) using a methanol extraction from freeze-dried and ground leaf discs, collected after a 2-h dark period. Dry leaf mass per unit area (DW^{-1}) was measured using leaf discs freeze-dried for 48 h.

Metabolite extractions

Leaves for all metabolite extractions were flash-frozen within the growth chamber taking care to prevent shade effects at midday. Metabolites for the metabolomic study were extracted from 5 mg of freeze-dried, ground leaves using boiling water as previously described (Cocuron et al., 2014; Cocuron and Alonso, 2014). Internal standards, 100 nmol of [U-^{13}C]glucose, 50 nmol of [U-^{13}C]glycine, and 10 nmol of [U-^{13}C]fumarate, were added at the time of the extraction. After lyophilization, extracts were resuspended in 350 µL of double distilled, deionized H_2O and vortexed. To quantify sugars and sugar alcohols, 150 µL of the sample was loaded onto a 0.2 µm MF centrifugal device (Nanosep, New York, NY, USA). The remaining 200 µL was transferred to a 3 kDa Amicon Ultra 0.5 mL filtering device (Millipore, Burlington, MA) for the quantification of AAs, phosphorylated compounds, and OAs. Samples were centrifuged at 14,000×g for 45 min at 4°C. Photorespiratory intermediates were extracted for targeted studies from 10 mg of freeze-dried, ground laves using 200 µL H_2O at 100°C for 5 min. After centrifugation and collection of the supernatant, this step was repeated and the two supernatants were combined for a final volume of ~ 400 µL. Extractions for enzymatic assays were performed on 50 mg of fresh weight ground leaves as previously described (Gibon et al., 2004).

Quantification of intracellular metabolites and enzymatic rates

For the metabolomic work, intracellular metabolite levels (AAs, OAs, phosphorylated compounds, sugars, and sugar alcohols,) were quantified using ultrahigh-performance liquid chromatography (UHPLC) 1290 Infinity II from Agilent Technologies (Santa Clara, CA, USA) coupled with a 5500 QTRAP mass spectrometer (LC-MS/MS) from AB Sciex Instruments (Framingham, MA, USA) as previously reported (Cocuron et al., 2014) with minor modifications. Briefly, for sugars and sugar alcohols quantification, the extracts from leaves obtained after centrifugation in Nanosep MF filter were diluted 100X in acetonitrile/water

(60:40, v/v) solution, then 5 µL of the diluted sample was injected onto the LC-MS/MS column. For AAs, the filtered extracts were diluted 50X in 1 mM hydrochloric acid, and 2.5 µL of the diluted sample was analyzed by LC-MS/MS. In order to quantify phosphorylated compounds and OAs, the filtered extracts were diluted 10X in ultra-pure water, and 10 µL was injected onto the column. LC-MS/MS data were acquired and processed using Analyst 1.6.1 software. The quantification of each intracellular metabolite was performed: i) using [U-$^{13}C_4$]fumarate, [U-$^{13}C_2$]glycine, and [U-$^{13}C_6$]glucose as internal standards to account for any loss of material during sample extraction and preparation; and ii) by correlating the resulting peak area of each metabolite with its corresponding external standard injected at a known concentration.

Targeted quantification of photorespiratory intermediates glutamine (Gln), glutamate (Glu), Ser, and Gly was performed by enzyme-coupled fluorescence assays with Amplex Red. Standard curves were created from 0 to 100 uM in H_20 for each metabolite. Gln samples in duplicate were prepared by treating 10 µL of extracted AAs and standard curve with 10 µL of 2.7 U of glutaminase (Megazyme, Bray, Ireland) in 40 mM NaAcetate, pH = 4.9 for 20 min at 37℃. On the same 96-well plate, duplicated 10 µl Glu samples and standard curve were mixed with 10 µL 40 mM NaAcetate, pH = 4.9. Fluorescence was evolved in 180 µL of 0.25 U/mL horseradish peroxidase (HRP), 27.8 mU/mL glutamate oxidase, and 0.1 mM Amplex Red in 100 mM Tris pH=7.5 for 30 min. In separate wells, paired Glu samples were treated with 180 µL containing 0.25 U/mL HRP and 0.1 mM Amplex Red in 100mM Tris pH=7.5 for 30 min. Fluorescence was quantified (Tecan, Männedorf, Switzerland) at an excitation of 545 nm, bandwidth 10 nm, and emission detection at 590 nm, bandwidth 5 nm. Ser samples in duplicate were prepared by treating 10 µL of extracted AAs and standard curve with 10 µL of 32 µU L-SER racemase, 40 µM pyridoxal 5′-phosphate (PLP), and 50 mM NaCl in 50 mM KPO_4, pH = 7.4 for 30 min at 37℃. Negative control samples were treated identically except L-Ser racemase was absent. Fluorescence was evolved in 180 µL of 10 µU of D-Ser dehydratase, 20 µM PLP, 5 µM $ZnCl_2$, 0.25 U/ml HRP and 0.1 mM Amplex Red in KPO_4, pH = 7.4 + 50 mM NaCl for 30 min at 37℃. Gly was quantified in duplicate, along with standard curve samples, by combining 10 µL of extracted AAs with 180 µL 3.5 mU GLY oxidase, 0.25 U/ml HRP, and 0.1 mM Amplex Red in 20 mM KPO_4, pH = 9, 100 mM NaCl, and 10% glycerol (v/v) for 30 min at 37℃. Negative controls were treated identically except Gly oxidase was absent.

Enzymatic rates for Gln synthetase (GS) and ferredoxin-glutamine-oxoglutarate glutamine transferase (Fd-GOGAT) were measured as previously described (Gibon et al., 2004) with minor modifications that 20 µL of the extract was used and specifically for GS, the catalytic rate was quantified after stabilizing for 5 min.

Results

Variation in acclimation of photosynthetic capacity to HL among ecotypes

LL-grown plants of the model *A. thaliana* ecotype Col-0 and two ecotypes locally adapted to contrasting environments (IT and SW) were shifted into HL, and photosynthetic capacity measurements were taken over 10 days along with measurements of the Q_A redox state, as quantified by the chlorophyll fluorescence parameter q_L. A statistically significant increase in q_L, when measured in saturating light, preceded the increase in photosynthetic capacity (q_L on Day 3 vs. ETR_{max} and P_{max} on Day 4) (Fig. 1A). The fastest rate of increase in q_L occurred between HL Day 1 and Day 3, whereas photosynthetic capacity on a leaf area basis (m^{-2}) rose most sharply between HL Day 4 and Day 6. In contrast, the increase in photosynthetic capacity plateaued at Day 4 when normalized by DW^{-1}, a proxy for leaf thickness. This indicates that by HL Day 6, leaves that had developed in HL showed the anticipated increase in leaf thickness (Stewart et al., 2017). The fastest rate of increase in P_{max} normalized by DW^{-1} (i.e., leaf thickness-independent increases in photosynthetic capacity) was between Day 3 and Day 4 of the post-HL shift (Fig. 1A).

While the three ecotypes shared a similar response of q_L and photosynthetic capacity to the shift to HL growth, the SW ecotype acclimated to HL growth condition faster than the other two ecotypes (Fig. 1B-D, S2). In particular, the SW ecotype on HL Day 3 and 4 had higher photosynthetic capacity relative to the other two ecotypes. Post-HL shifted SW ecotype plants also achieved the highest P_{max} normalized by DW^{-1} (Fig. S2D). The more rapid acclimation of the SW ecotype was also observed when q_L was measured using the growth light intensity (Fig. S2E). In contrast to q_L at saturating light, q_L at the growth light intensity significantly increased in both the Col-0 and SW ecotypes on HL Day 1, with the larger magnitude increase in the SW ecotype (Fig. S2E). Thus, it is concluded that the SW ecotype possesses a more robust initial phase of the photosynthetic capacity acclimation response relative to the Col-0 and IT ecotypes.

To map the natural diversity of the photosynthetic acclimation response to HL in greater detail, HL shifts were performed on LL-grown plants of the geographically and phenotypically diverse genome-sequenced *A. thaliana* ecotype population first assembled by Cao et al. (Cao et al., 2011). HL Day 4 was selected as an optimal point to test ecotypic variation in the acclimation of photosynthetic capacity to HL due both to the strong acclimation of photosynthetic capacity in the SW ecotype relative to Col-0 and IT and the absence of changes in DW^{-1} in those three ecotypes at that time point (Fig. 1, S2). A range of fold changes in photosynthetic capacity (HL Day 4/LL) was observed with a low of ~0.95 to a high of ~2.2-fold (Fig. 2). Ecotypes that showed strongly increased photosynthetic capacity, such as Dog-4 (ecotype #5), had a fold change in photosynthetic capacity that exceeded the fold change of the SW ecotype when quantified by either ETR_{max} or P_{max}. At the opposite extreme, some ecotypes when the fold change in photosynthetic capacity (HL Day 4/LL) was measured by either ETR_{max} or P_{max} showed virtually no change or even a slight decline in HL, best exemplified by the ecotypes Bak-2 and Lago-1 (ecotypes #70 and #78, respectively).

Chlorophyll per unit area on average decreased to ~75.7% in HL-shifted plants relative to LL with extremes of slight induction in chlorophyll per unit area for ecotypes such as Shigu-1 and Stephn-2 (ecotypes #43 and #11, respectively) and a greater than 2-fold reduction in chlorophyll per unit area for ecotypes such as Don-0 and Leb-3 (ecotypes #23 and #25, respectively) (Fig. S3). Importantly, no correlation was observed between chlorophyll per unit area and ETR_{max} values (Fig. S3). This verifies that the use of chlorophyll per unit area values in HL Day 4 plants and LL as a means to estimate light absorptance for use in the calculation of the fold change in ETR_{max} did not systematically bias these calculations (see Materials & Methods for details on the estimation of ETR_{max} values).

The fold change in photosynthetic capacity (HL Day 4/LL) quantified by P_{max} and ETR_{max} across the population was tightly correlated (Fig. 2B, $R^2 = 0.3799$). Similarly, the fold change in q_L (measured in saturating light) was also correlated with the fold change in ETR_{max} (Fig. S3, $R^2 = 0.2062$), consistent with the increase in photosynthetic capacity contributing to the restoration redox poise of the PET chain in HL-shifted plants. The correlation was weaker between ETR_{max} and P_{max} or q_L for LL-grown plants relative to these same comparisons made in HL-shifted plants (Fig. 2C-D, Fig. S4). The average increase in photosynthetic capacity, calculated from all the ecotypes, as measured by ETR_{max} ($ETR_{max\ HL}/ETR_{max\ LL} \approx 1.66$) was higher than the average fold

change of photosynthetic capacity as quantified by P_{max} ($P_{max\ HL}/P_{max\ LL} \approx 1.48$). Precise measurement of ETR_{max} necessitates direct quantification of values that are only indirectly estimated in this work due to the scale of phenotyping(McClain and Sharkey, 2020; Loreto et al., 2009; Evans et al., 2017; Evans, 1996). Hence, in some cases the ETR_{max} reported here may overestimate the fold change in photosynthetic capacity due potentially to changes in, for instance, PSII-to-PSI state transitions, or carotenoid contributions to light absorptance. The alternative and mutually non-exclusive possibility is that P_{max} can underestimate PET rates due to oxygen-consuming pathways, while significantly repressed, persisting in saturating CO_2 (Carrier et al., 1989).

In this context, it is worth noting the several outlier ecotypes that had ETR_{max} values that strongly contrasted with P_{max} values under one of the growth conditions. For instance, ecotypes such as Voeran-1 (ecotype #9), Shigu-2 (ecotype #15), and TueV-13 (ecotype #21) strongly increased photosynthetic capacity when quantified by ETR_{max} but had a moderate or no increase in P_{max} following the HL shift (Fig. 2B-D). Specifically, this was a consequence of low P_{max} values relative to ETR_{max} when measured in the HL-shifted plants for these three ecotypes. Whereas the majority of ecotypes showed quite similar P_{max} and ETR_{max} values, it would make an interesting case study to investigate what specific mechanisms underlie the growth condition-specific divergence of ETR_{max}, as estimated in this work, and P_{max} values in ecotype such as Vorean-1.

Impact of the HL shift on the leaf metabolome

In order to identify the metabolic changes linked to the increase in photosynthetic capacity during the HL shift, metabolomic data were collected for the SW ecotype, a strongly acclimating ecotype, and Col-0, a weakly acclimating ecotype. A principal component (PC) analysis of HL-shifted and LL-grown plants for both ecotypes separated both Col-0 from SW plants and HL- from LL-plants on the principal component 1 (PC1) axis (Fig. S5A). A PC analysis of just SW plants separated HL-shifted plants from LL-grown along PC1 and then separated along the time-axis of the HL treatment on PC2 (Fig. S5B). Thus, the metabolomes could be reliably resolved by ecotype, growth condition, and the time component.

Broadly, sugar-phosphates, sugars, and AAs had increased abundance in HL-shifted plants (Fig. 3, best illustrated by the left set of columns). The exceptions to this overall trend of

increased abundance in HL-shifted plants included the decreased abundance of the AAs lysine (Lys), the photorespiratory intermediate Ser, threonine (Thr), as well as in the SW ecotype the glycolytic intermediate phosphoenolpyruvate (PEP) (Fig. 3, best illustrated by the left set of columns). AAs, as a class of metabolites, increased over time in response to the HL shift driven primarily by the increase over time of the high abundance Glu- and Gln-derived AAs (Fig. 3, best illustrated by the left set of columns). The high abundance foliar metabolites to have the inverse profile, decreasing abundance over time in response to the HL shift, were intermediates of the CBB cycle and sucrose biosynthesis (fructose 1,6-bisphosphate (FBP), sucrose 6-phosphate (Suc6P), and ribulose 1,5-bisphosphate (RuBP)), the TCA cycle (fumarate, isocitrate, and α-ketoglutarate), as well as the AAs Thr and Ser (Fig. 3, best illustrated by the middle set of columns). In contrast to the temporal response of AAs, soluble sugars reached their highest abundance on HL Day 1 driven by a transient increase in Glc and Fru levels, whereas Suc levels remained at an elevated abundance throughout the post-HL shift period (Fig. 3, best illustrated by the middle set of columns).

Variable importance (VIP) analyses of the supervised partial least-squares discriminant analysis (PLSDA) were performed in order to identify metabolites that differentiate the HL metabolomes of these ecotypes relative to their paired LL metabolome. In the SW ecotype, VIP analysis identified Gln, both a photorespiratory intermediate and product of N assimilation, as the strongest metabolomic differentiator of HL-shifted plants from LL-grown plants (Fig. 4A, Fig. S5C). Similarly, both Gln and Gly, another key photorespiratory intermediate, were among the highest VIP scores between HL-shifted and LL-grown plants in the Col-0 ecotype (Fig. 4B, Fig. S5D). When the results of the SW VIP analysis were compared to the results of the Col-0 analysis, the higher scoring metabolites in the SW VIP analysis relative to the Col-0 analysis included ATP, valine (Val), histidine (His), Glu-derived AAs γ-aminobutyric acid (GABA) and proline (Pro) as well as phosphoenolpyruvate (PEP), which was one of few components of central metabolism with decreased abundance in the HL-shifted SW plants. Likewise, the metabolites which scored more strongly in the post-HL vs. LL VIP analysis of Col-0 relative to the SW analysis included Suc6P, ADP-glucose, RuBP, sedoheptulose 7-phosphate (S7P), the AAs phenylalanine (Phe), tryptophan (Trp), aspartate (Asp), and Gly, as well as the glucose (Glc) and fructose (Fru). Increased abundance of metabolites with high VIP scores specifically in the strongly acclimating SW ecotype such as ATP and Glu-derived residues, as well as decreased

PEP, represent putative metabolic indicators of efficient photosynthetic capacity to HL. Likewise, high VIP scores specifically in the weakly acclimating Col-0 ecotype, such as increased abundance of Suc6P and ADP-glucose, may represent indicators of inefficient photosynthetic capacity acclimation to HL.

As a final means of linking specific metabolites to the change in photosynthetic capacity, the abundance over time of metabolites in the SW ecotype was correlated with the change in photosynthetic capacity (Fig. 5). Levels of Glu, Gln, and other Glu-derived AAs such as GABA and Pro were positively correlated with photosynthetic capacity. Additionally, the Asp-derived AAs homoserine and methionine (Met) were positively correlated with photosynthetic capacity whereas the Asp-derived AA Thr was inversely correlated. The two strongest inverse correlations were for fumarate and Ser. The correlation with photosynthetic capacity of Glu- and Gln-derived AAs, products of N assimilation, highlights the relationship of this pathway with the acclimation of photosynthetic capacity to HL. The decreased abundance of metabolites involved in the supply of OAs to support N assimilation (e.g., PEP, fumarate, isocitrate, α-ketoglutarate) also fits with the importance of N assimilation rates to increased photosynthetic capacity (Fig. S1A). The strong inverse correlation of photosynthetic capacity with Ser levels and elevated Gly abundance in HL-shifted plants also indicate elevated photorespiration rates (Fig. S1B). The links between photorespiration, N assimilation, and the acclimation of photosynthetic capacity to HL were explored further in subsequent experiments.

Metabolic signatures of primary N assimilation and photorespiration in HL

The SW ecotype also differed from the Col-0 and IT ecotypes in two physiological parameters relevant to photorespiration rates during the HL shift, stomatal conductance (g_s) and the post-illumination CO_2 burst (PIB) (Fig. S6). Lower g_s in HL will reduce intracellular CO_2 levels, promoting higher rates of photorespiration. g_s decreased in all three ecotypes on HL Day 1, but on HL Day 3, the SW ecotype was the sole ecotype to restore pre-shift g_s levels (Fig. S6). However, the percentage increase in the net CO_2 assimilation rate by measuring in low O_2 air, used to repress photorespiration during gas exchange analysis, relative to ambient O_2 air did not statistically differ between the ecotypes (Fig. S6), indicating that the impact of g_s on Rubisco oxygenation rates was not drastic. Downstream of Rubisco oxygenation, the magnitude of the PIB, which estimates mitochondrial GDC enzymatic capacity, increased in all three ecotypes on

Day 10 of the HL shift but was increased solely in the SW ecotype on Day 3 (Fig. S6). This supports that SW may have had higher photorespiratory capacity early in the HL shift relative to the other two ecotypes.

Whether photorespiration and primary N assimilation caused the increase in Gly and Gln levels, respectively, in HL-shifted plants was investigated by decoupling rates of these processes from the shift to HL growth conditions by combining this treatment with introducing low O_2 air into the growth chamber. An increased Gln/Glu was observed in SW, Col-0, and IT plants on HL Day 1 in ambient O_2 conditions with the highest Gln/Glu ratio in the SW ecotype (Fig. 6A). In contrast, at HL Day 3 in low O_2 air, the Gln/Glu ratio decreased in all three ecotypes relative to the LL value. The total pool of Gln + Glu also increased in HL-shifted plants in ambient air and again, this increase was not observed in low O_2 air (Fig. 6B). The Gly/Ser ratio, as well as the total pool of Gly + Ser, were also increased after the HL shift in ambient O_2 levels in all three ecotypes and not in low O_2 air (Fig. 6C-D).

While these trends are shared between the ecotypes, the Gly/Ser and Gln/Glu ratios did not behave identically in all three ecotypes. For example, the Gln/Glu ratio in ambient O_2 conditions was consistently higher in the SW ecotype, whereas on Day 1 of the HL shift, the Gly/Ser ratio was lowest in the SW ecotype. Thus, the HL-driven increase in Gln/Glu and Gly/Ser, metabolic markers for the rates of N assimilation and photorespiration, respectively, was dependent on ambient O_2 levels and significant differences between ecotypes for these metabolic markers could be measured on HL Day 1.

Correlating metabolic signatures of N metabolism with the induction of high photosynthetic capacity in HL

As metabolic indicators of N assimilation and photorespiration rates, levels of Gln, Glu, Ser, and Gly, as well as the activity of enzymes GS and Fd-GOGAT (key to both primary N assimilation and photorespiration), were quantified on HL Day 1 using the full ecotype panel. The goal was to correlate changes in these metabolites on HL Day 1 with the fold change in photosynthetic capacity measured on HL Day 4. Strongly supporting a link between photorespiration and N assimilation rates early in the HL shift and the later increase in photosynthetic capacity, both the Gln/Glu and Gly/Ser ratios on HL Day 1 were positively and strongly correlated with the fold change in photosynthetic capacity on HL Day 4 (HL Day 4/LL)

when measured as ETR_{max} and correlated, albeit not as strongly, with P_{max} (Fig. 7A-B, Table 1, Fig. S6, R^2 = 0.5292 and 0.1193, respectively, for Gln/Glu, and R^2 = 0.4034 and 0.0693, respectively, for Gly/Ser). The positive correlation between the fold change in photosynthetic capacity and the Gly/Ser ratio in the larger ecotype panel contrasted with the behavior of the smaller ecotype set of SW, Col-0, and IT plants (Fig. 6C). Additional correlations were found in this dataset, albeit none as strong as the correlation for ETR_{max} and Gln/Glu and Gly/Ser values. ETR_{max} values in HL-shifted plants were weakly positively correlated with both the Gln/Glu and Gly/Ser ratios (Table 1, Fig. S7A-B, R^2 = 0.1408 and 0.1670, respectively), whereas photosynthetic capacity in LL-grown plants was weakly negatively correlated with the fold change in photosynthetic capacity (Table 1, Fig. S7C-D, R^2 = 0.1155 and 0.0536, respectively). The total Gly + Ser pool in HL-shifted plants was correlated with the fold change in photosynthetic capacity as measured by ETR_{max}, as well as weakly negatively correlated with ETR_{max} for LL-grown plants (Fig. 7B, Fig. S7C, R^2 = 0.1562 and 0.0559, respectively), again supporting a link between photorespiratory capacity and the later increase in photosynthetic capacity. In contrast to the Gly + Ser result, the total pool of Gln + Glu was not correlated with the induction of photosynthetic capacity (Table 1). GS enzymatic activity on HL Day 1 was also weakly correlated with the fold change in the photosynthetic capacity as measured by ETR_{max} and was negatively correlated with ETR_{max} for LL-grown plants (Fig. 7C, Fig. S7D, R^2 = 0.1190 and 0.1171, respectively). GS activity is necessary for both photorespiration and primary N assimilation, thus plants with high GS activity may be indicative of either or both high photorespiratory and primary N assimilatory capacity. Similarly, GS activity on HL Day 1 was correlated with the fold change in q_L and was weakly negatively correlated with q_L for LL-grown plants (Fig. S8, R^2 = 0.1254 and 0.0526, respectively). In summary, metabolic indicators of N assimilation, N assimilation/photorespiration enzyme activities, and metabolic indicators of photorespiration rates early in the HL shift were positively correlated with the magnitude of the subsequent increase in photosynthetic capacity measured at HL day 4

Manipulating N metabolism using O_2 levels and impact on the induction of high photosynthetic capacity in HL

Two models can be envisioned for the relationship between increased photosynthetic capacity and photorespiration/N assimilation rates. First, high rates of N assimilation and

photorespiration might generate a positive signal for photosynthetic capacity acclimation and a HL shift in low O_2 air should block the increase in photosynthetic capacity. Second, low photorespiratory rates could repress photosynthetic capacity acclimation to HL. To test this scenario, ecotypes selected to cover the full range of diversity in fold change of photosynthetic capacity were shifted into HL combined with low O_2 air and O_2 oxygen air (Fig. 8). Two mutants affecting photorespiratory enzymes, Ser hydroxymethyltransferase (*shm1*, AT4G37930) and Fd-GOGAT (*gls1-30*, AT5G04140) (Somerville and Ogren, 1981, 1980; Coschigano et al., 1998; Somerville and Ogren, 1982), were also included in this experiment to test the response of photosynthetic capacity to HL in genotypes with extremely low photorespiratory capacity.

In low O_2 air (2% O_2), the increased photosynthetic capacity at HL Day 4 was on average slightly greater than the fold change in ambient O_2 (Fig. 8A). In contrast, high O_2 air (30% O_2) blocked the increase in photosynthetic capacity at HL Day 4. These results are inconsistent with the first model that high photorespiratory/N assimilation rates act as a positive signal necessary for the licensing of photosynthetic capacity acclimation in HL. In fact, this experiment strongly supports the second model (that low photorespiratory rates repress photosynthetic capacity acclimation). For instance, non-acclimating and weakly acclimating ecotypes, such as Lago-1 (ecotype #79), Col-0, IT, Yeg-1 (ecotype #74), as well as the two photorespiratory mutants, increased photosynthetic capacity specifically in low O_2 air on HL Day 4 (Fig. 8A-B), a condition where photorespiration was repressed. Both Yeg-1 and Lago-1 are among the ecotypes with the lowest measured GS values on HL Day 1 (Fig. 7D), suggesting that like the photorespiratory mutants, these ecotypes may have low photorespiratory capacity. Thus, insufficient photorespiratory capacity appears to have a repressive effect on the acclimation of photosynthetic capacity to HL and certain weakly acclimating ecotypes are only able to increase photosynthetic capacity in HL under non-photorespiratory conditions.

Unlike at ambient O_2 levels, increased photosynthetic capacity in HL was not sustained in low O_2 at HL Day 7 (Fig. 8B). Measurements collected for the Col-0, IT, and SW ecotypes at HL Day 7 revealed that photosynthetic capacity precipitously declined in the low O_2 air, whereas in ambient O_2 photosynthetic capacity increased for all three ecotypes (Fig. 8B). For the photorespiration mutants and all genotypes in high O_2 air, reliable photosynthetic measurements could not be recorded at HL Day 7 due to wilting and chlorosis. This was an anticipated result

given the long-term imbalance in C/N-metabolism (i.e., high carboxylation rates, low nitrogen assimilation) in low O_2 air-grown plants by HL Day 7.

Discussion

Ecotypic variation in the acclimation of photosynthetic capacity to HL

Overall, a similar temporal pattern of Q_A redox state and photosynthetic capacity was observed among the Col-0, IT, and SW ecotypes in response to the shift from LL to HL (Fig. 1, S2). Initially, the Q_A redox state, as measured by qL, was strongly reduced on Day 0 and began to recover (i.e., become more oxidized) when measured using the growth light intensity on HL Day 1. In contrast, significantly increased q_L at saturating light was not detectable until HL Day 3, and increased photosynthetic capacity was not detectable until HL Day 4. By Day 6 of the HL shift, leaves that had developed in HL had fully emerged, and these thicker leaves, as indicated by increased DW, showed strongly increased photosynthetic capacity per unit area (Stewart et al., 2017; Athanasiou et al., 2010). In terms of differences between the ecotypes, the SW ecotype was the first to increase photosynthetic capacity (observable at HL Day 3) and experienced the greatest increase in q_L in the early phase of the HL shift (observable at HL Day 1). This efficient response to HL fits with prior data suggesting that the SW ecotype (relative to the IT ecotype) is more strongly HL adapted (Stewart et al., 2017). In the context of the metabolic data, a likely explanation for early recovery of Q_A redox poise in the SW ecotype is the efficient acclimation of photosynthetic and N metabolism after shifting to HL, thus preventing feedback inhibition of PET (Demmig-Adams et al., 2014; Paul and Pellny, 2003; Pammenter et al., 1993). This likely included both more strongly enhanced fluxes through pathways at the intersection of C and N metabolism in HL (e.g. photorespiration and primary N assimilation) as well as more efficient flux through triose-phosphate assimilation pathways, as discussed in greater detail below, relative to the Col-0 and IT ecotypes.

A continuous distribution of photosynthetic capacity acclimation values (HL Day 4/LL) with fold changes of ~0.95 to 2.2 was measured using the larger ecotype panel (Cao et al., 2011) (Fig. 2). While many ecotypes efficiently increased photosynthetic capacity by HL Day 4, the strongest acclimating ecotypes did not geographically cluster. For instance, strongly acclimating ecotypes included the SW ecotype (latitude- 62°N), Dog-4 (Turkey, ecotype #5, latitude- 41.07°N), Star-8 (Germany, ecotype #25, latitude- 48.43°N), and Rovero-1 (Italy, ecotype #8,

latitude- 46.25°N). This was not an unanticipated result. Ecophysiological studies of photosynthetic capacity acclimation to HL have suggested that adaptation to local growth environment is the major determinant of the strength of this response and in particular, plants that are dual-adapted to thrive in both shaded and full sunlight environments appear to have the largest dynamic range in photosynthetic capacity in response to light levels (Murchie and Horton, 1997; Bjorkman and Holmgren, 1963). Thus, it is our prediction that the weakly acclimating ecotypes identified here represent shade-adapted *A. thaliana* ecotypes, whereas the strongly acclimating ecotypes are those ecotypes able to thrive in full sunlight growth conditions and perhaps are also dual-adapted for growth in shade and full sun (Athanasiou et al., 2010).

Parallels exist in the acclimation of photosynthetic capacity to cold and HL (Strand et al., 1999; Huner et al., 2012). There was a weak effect of latitude on photosynthetic capacity acclimation in this study. The 12 northern latitude ecotypes (> 50°N) had a larger HL/LL fold change in photosynthetic capacity (1.75 for ETR_{max} and 1.57 for P_{max}) relative to the 16 southern latitude ecotypes (< 40°N, 1.61 for ETR_{max} and 1.39). Exceptionally high photosynthetic capacity per unit area can be achieved by combining HL and cold growth conditions (Demmig-Adams et al., 2018; Cohu et al., 2013). It seems likely that latitudinal effects on photosynthetic capacity would be stronger using a combination of cold and HL during growth as opposed to treatment with only HL, the latter being the condition that most strongly favors the photoprotective contributions of photorespiration to HL acclimation (Savitch et al., 2000; Ma et al., 2014).

Metabolic acclimation to HL growth conditions that increase photosynthetic capacity

Changes to three metabolic pathways are particularly noteworthy as photosynthetic capacity increased over the time course of the HL shift (Fig. 3-5). First, evidence for an increased rate of primary N assimilation in HL-shifted plants can be found in the increased abundance of Glu-derived AAs and the progressively increasing Gln/Glu ratio (Foyer et al., 2003). HL-shifted plants produce reducing equivalents in the light at an accelerated rate, and primary N assimilation may act as an important electron sink under these conditions(Foyer et al., 2003; Osmond et al., 1997). Total AA abundance increased over time in the HL-shifted plants, primarily driven by the change in the abundance of Gln and other Glu-derived AAs. The abundance of Glu is tightly regulated in plants, but nonetheless, Glu increased on HL Day 6 and

Day 10 in concert with the largest jumps in photosynthetic capacity measured on a leaf area basis (Foyer et al., 2003; Huppe and Turpin, 1994; Florian et al., 2013).

Increased rates of Gln synthesis in HL-shifted plants depend on a constant supply of α-ketoglutarate carbon skeletons. α-ketoglutarate levels, which constituted just 0.5% of the total OA pool, gradually declined in HL over the time course as photosynthetic capacity increased. There is evidence in the metabolomic data for two sources of OAs to maintain the α-ketoglutarate supply to chloroplasts that would have been necessary to support enhanced primary N assimilation rates. These are enhanced *de novo* OA synthesis, particularly notable on HL Days 1 and 3, and the drawing down of the existing OA pool in the leaf, particularly notable on HL Days 6 and 10. PEP carboxylase activity, which converts the glycolytic intermediate PEP into the OA oxaloacetate, was increased, and PEP abundance decreased in HL-shifted SW plants. In concert, the size of the total OA pool increased slightly on HL Day 1 and 3, despite elevated AA synthesis rates. In both Col-0 and SW, trehalose-6P was induced in the HL-shifted plants. Trehalose-6P signals the repression of sucrose synthesis and enhances OA synthesis rates via activating PEP carboxylase activity (Figueroa et al., 2016). Consistent with this role for trehalose-6P, levels of sucrose biosynthesis intermediates (FBP, F6P, G6P, and Suc6P) dramatically increased in both ecotypes on Day 1 of the HL shift, and subsequently, FBP and Suc6P levels each declined on Day 3 and continued to decline for the rest of HL-shift period. The elevated FBP levels on Day 1 and Day 3 also may have allosterically activated pyruvate kinase, further contributing to the accelerated OA synthesis rates (Huppe and Turpin, 1994; Plaxton and McManus, 2006). While there is evidence consistent with trehalose-6P acting to support accelerated OA synthesis rates in HL, weaker HL-acclimating genotypes often induce higher levels of trehalose-6P than stronger acclimating ones, as observed here by the stronger induction of trehalose-6P in Col-0 than in the SW ecotype. Thus, a direct role for trehalose-6P in signaling changes in photosynthetic capacity in HL remains unlikely(Paul, 2007; Dyson et al., 2015).

Later in the time course, OA levels dropped on HL Day 6 and then again on HL Day 10, driven predominantly by declining fumarate abundance and to a lesser extent isocitrate and α-ketoglutarate. Thus, the AA/OA ratio shifted from 0.88 in LL-grown plants to 3.33 on HL Day 10. In the extreme, the Gln/fumarate ratio was 0.28 in LL-grown plants (fumarate constituted 35% of the total OA pool in LL-grown plants) increased to 13.14 by HL Day 10. High fumarate

levels are necessary for the rapid assimilation of exogenous N in *A. thaliana* (Pracharoenwattana et al., 2010). Taken together with the early induction of enhanced OA synthesis rates, a shift may have occurred over the HL time course in how carbon skeletons were primarily supplied to support high primary N assimilation rates. At the early stage of HL acclimation, accelerated flux through the anaplerotic reaction was primarily responsible for supplying carbon skeletons for N assimilation, however, once photosynthetic capacity began to increase, flux through the anaplerotic reactions appeared to decline despite the plant maintaining higher levels of primary N assimilation.

The second pathway to highlight, and necessarily intertwined with the discussion of primary N assimilation in HL, was the impact of increased photorespiration on the metabolome of HL-shifted plants. The shift to HL in the Col-0, IT, and SW on HL Day 1 decreased g_s, which would increase photorespiration rates. The Gly/Ser ratio increased from 0.55 in LL-grown SW plants to 2.6 on HL Day 10, as a consequence of both progressively increasing Gly levels and declining Ser levels. Enhanced photorespiratory and nitrate assimilation rates are linked (Bloom et al., 2002; Rachmilevitch et al., 2004; Busch et al., 2018) and consistent with the observation here of the complete suppression of the HL-induced increase in Gly/Ser (a metabolic indicator of photorespiration) and Gln/Glu (a metabolic indicator of primary nitrogen assimilation) in low O_2 (Fig. 6). Under high photorespiratory conditions, the conversion of excess sugar phosphates into the AAs Gly and Ser may provide an important photoprotective valve, however, the largest magnitudes of AA changes observed during HL acclimation in this work were the increases in Gln and Glu-derived AAs. Thus, while an abundance of evidence points to co-induction of N assimilation and photorespiration in HL, more insights remain to be discovered on the regulatory links between photorespiration and N assimilation in HL.

Finally, the sugar biosynthesis pathways must be highlighted. Sugar phosphates and sugars in Col-0 and SW ecotype, in particular on HL Day 1, both increased but to a lesser extent in the stronger acclimating SW ecotype. Notably, the Fru + Glc level was induced 2.6-fold on HL Day 1 in SW plants and ~1.5 fold on the subsequent sampling days, whereas Fru + Glc was 6.7-fold induced in Col-0 on HL Day 1. Sucrose, starch, CBB cycle, and glycolysis intermediates were all at higher levels on HL Day 1 in the Col-0 ecotype relative to SW. Furthermore, the increase in ATP/ADP ratio which occurs in the SW ecotype in HL was not observed in the Col-0 ecotype. These results are consistent with higher levels of sink limitation in the Col-0 ecotype

relative to the SW ecotype following the HL shift and thus weaker acclimation of photosynthetic capacity to HL in this ecotype (Demmig-Adams et al., 2017; Häusler et al., 2014; Goldschmidt and Huber, 1992; Paul and Pellny, 2003; von Schaewen et al., 1990). In total, the model that can be drawn from these combined metabolomic insights of the strongly acclimating SW ecotype and initially weakly acclimating Col-0 ecotype is one where increased photosynthetic capacity during the early phases of HL acclimation depends on a combination of high N assimilation, photorespiration, and efficient sink utilization of photosynthate (Fig. 9).

High primary N assimilation and photorespiration rates correlate with the increase in photosynthetic capacity in HL

Rates of primary N assimilation and photorespiration, as measured by Gln/Glu and Gly/Ser, respectively, were strongly correlated with the fold change in photosynthetic capacity on HL Day 4 measured as ETR_{max} (Fig. 7). GS enzymatic activity also correlated, albeit not as strongly, with the fold change in photosynthetic capacity, an indicator that maximum capacity for primary N assimilation and photorespiration (not just simply rates of these processes) was also higher in plants that went on to increase photosynthetic capacity at HL Day 4. The total Ser + Gly pool, largely driven by the increase in Gly, also correlated with the induction of photosynthetic capacity. This also supports the conclusion that plants with high photorespiratory capacity early in the HL shift are more likely to induce high photosynthetic capacity in response to the shift to HL growth. Again, it is worth emphasizing that primary N assimilation and photorespiration rates in HL are tightly linked as manifested here in the shared behavior of the Gly/Ser and Gln/Glu levels and as previously described (Bloom et al., 2002; Rachmilevitch et al., 2004; Busch et al., 2018).

Lower C/N ratios are also linked to higher photosynthetic capacity leaves and thus, the early induction of high N assimilation rates in plants that increase photosynthetic capacity at HL Day 4 can maintain a lower C/N ratio (Givnish, 1988; Evans and Poorter, 2001; Paul and Pellny, 2003). In fact, in the metabolomic data, sugar and sugar-phosphate levels are higher and AAs are lower in the weakly acclimating Col-0 relative to the strongly acclimating SW ecotype on HL Day 1, reflecting the imbalance in C/N in Col-0 at the beginning of the HL shift relative to SW (Fig. 3). N assimilation rates in HL are proportional to the rate of PET(Foyer et al., 2003), and thus the correlation between Gln/Glu values on HL Day 1 and the fold change in the increase of

photosynthetic capacity (Fig. 7) would seem to suggest that the increased photosynthetic capacity is predicted by high rates of PET early in the HL shift (Fig. 9). In this model, ecotypes that did not increase primary nitrogen assimilation and photorespiratory rates early in the HL shift would be those that exhibited low PET rates early in the HL shift, as photorespiration and N assimilation represent key pathways for restoring Q_A redox poise (Fig. 9). Further, the C/N ratio will rapidly increase in these weakly acclimating plants due to low N assimilation rates, as exemplified by the Col-0 metabolomic data (Fig 3), and sugar signals in excess of nitrogen can act as negative feedback signal on photosynthetic capacity (Paul & Pellny, 2003).

Two models can be envisioned for the signaling relationship between photorespiration and photosynthetic capacity acclimation to HL. The first is that high photorespiration rates act as a positive metabolic signal that licenses an increase in photosynthetic capacity. The second is that low photorespiratory rates act as a repressive signal that blocks photosynthetic capacity acclimation to HL. Consistent with this second model, high 2-phosphoglycolate (2-PG) acts as a potent inhibitor of the CBB cycle in photorespiration mutants (Flügel et al., 2017; Li et al., 2019), providing a potential mechanism for the repression of photosynthetic capacity acclimation in genotypes with low photorespiratory capacity. 2-PG levels were not quantified as a part of our metabolomics datasets and it has already been shown that 2-PG abundance does not increase in HL (Li *et al.*, 2019), which may be a consequence of homeostatic control of 2-PG levels. Measurement of photosynthetic capacity acclimation to HL in low O_2 air was consistent with this second model of repression of photosynthetic capacity acclimation by low photorespiration capacity (Fig. 8). All strongly acclimating ecotypes tested were able to induce photosynthetic capacity to similar magnitudes in low O_2 and ambient O_2 on HL Day 4. Furthermore, high O_2 air blocked the acclimation of photosynthetic capacity to HL in all ecotypes and genotypes tested. Surprisingly, some non-acclimating and weakly acclimating ecotypes in ambient O_2 conditions, exemplified by Lago-1 (ecotype #79), strongly induced high photosynthetic capacity specifically in low O_2 air. Photorespiratory mutants behaved similarly to Lago-1 with no induction of photosynthetic capacity in HL in ambient O_2 conditions but strong induction in low O_2 air. Given that Lago-1 and other non-acclimating ecotypes also had low GS levels, an indicator of both photorespiratory and N assimilatory capacity, and low Gly/Ser levels measured on HL Day 1, several independent lines of evidence indicate that the weak acclimation of ecotypes such as Lago-1 may be a consequence of low photorespiratory capacity. The weak acclimating Col-0 and

IT ecotypes behaved similarly to Lago-1 (Fig. 8). In addition to low GS activity, these ecotypes were also measured for PIB, which is proportional to the photorespiratory GDC activity, and PIB was lower in Col-0 and IT prior to HL Day 4 relative to the strongly acclimating SW ecotype (Fig. S6).

Thus, in ambient O_2 levels, the correlation of low photorespiration and N assimilation rates early in the HL shift in ecotypes with weak or no increase in photosynthetic capacity on HL Day 4 reflects the repression of flux through pathways by a negative signal that is absent in non-photorespiratory conditions (Fig. 7 & 9). In this framework, the correlation of GS levels and the fold change in photosynthetic capacity also take on new meaning. Low photorespiratory capacity early in the HL shift may lead to the transient build-up in early intermediates of photorespiration, setting off a homeostatic signal that simultaneously represses photosynthesis and photorespiration as previously described in the 2-PG photosynthesis control model (Flügel et al., 2017; Timm et al., 2016, 2019; Li et al., 2019). These results also suggest that one reason for the absence of a photosynthetic capacity acclimation response to HL in shade-adapted ecotypes may be decreased N-partitioning to enzymes of photorespiration, thus, preventing shade-adapted ecotypes from efficiently increasing photorespiratory rates upon exposure to HL. As expected, long-term maintenance of high photosynthetic capacity depended on increased N assimilation in HL and, likely C/N balancing as well, as elevated photosynthetic capacity in HL in low O_2 air precipitously declined by HL Day 7 (Fig. 8) (Priestley *et al.*, 1988; Kawasaki *et al.*, 2015).

In summary, the fold change of increased photosynthetic capacity on HL Day 4 was correlated with markers of primary N assimilation and photorespiration rates on HL Day 1 across a large panel of *A. thaliana* ecotypes (Fig. 7). Efficient flux through these pathways permits acclimating plants to maintain a relatively oxidized Q_A redox state early in the HL shift and high PET rates (Fig. 9). Flux entering the photorespiration pathway in excess of limited photorespiratory capacity causes feedback inhibition of PET and blocks the photosynthetic capacity acclimation response to HL. Thus, plants with high levels of photorespiratory and primary N assimilation enzymes on HL Day 1, capable of sustaining high rates of flux through these pathways, are able to limit feedback inhibition and efficiently acclimate photosynthetic capacity to HL. Limited photorespiratory capacity which impairs a plant's ability to acclimate to different growth light regimes may have detrimental effects on biomass productivity, which could be suppressed by the use of a photorespiratory bypass (South et al., 2019). In their work,

South et al. found that introduction of a photorespiratory bypass had positive effects on growth beyond modeled expectations (South et al., 2019). Future work on photosynthetic capacity acclimation should continue to push towards a mechanistic understanding of how the regulatory links between the pathways of central metabolism control photosynthetic capacity in response to growth environment signals. These insights will inevitably open up new targets for the optimization of photosynthesis in crop species and provide a better predictive framework for how engineered pathways will integrate with central metabolism.

Acknowledgments

We thank the BioAnalytical Facility at the University of North Texas for the support with mass spectrometry analysis, Dr. Olga Gaidarenko for the IR camera images and advice on IR-image analysis, and Dr. Setsuko Wakao and Dr. Masakazu Iwai for their comments on the preparation of this manuscript. This work was supported by the Gordon and Betty Moore Foundation through Grant GBMF 2550.03 to the Life Sciences Research Foundation [to C.R.B]. K.K.N. is an investigator of the Howard Hughes Medical Institute.

References

Anderson, J.M., Chow, W.S., and Goodchild, D.J. (1988). Thylakoid Membrane Organisation in Sun/Shade Acclimation. Funct. Plant Biol. **15**: 11–26.

Anderson, J.M. and Osmond, C.B. (1987). Shade-sun responses: compromises between acclimation and photoinhibition. In Photoinhibition, J.M. Anderson, C.B. Osmond, D.J. Kyle, and C.J. Arntzen, eds (Elsevier: Amsterdam), pp. 1–38.

Athanasiou, K., Dyson, B.C., Webster, R.E., and Johnson, G.N. (2010). Dynamic acclimation of photosynthesis increases plant fitness in changing environments. Plant Physiol. **152**: 366–373.

Bailey, S., Horton, P., and Walters, R.G. (2004). Acclimation of Arabidopsis thaliana to the light environment: the relationship between photosynthetic function and chloroplast composition. Planta **218**: 793–802.

Bailey, S., Walters, R.G., Jansson, S., and Horton, P. (2001). Acclimation of Arabidopsis thaliana to the light environment: the existence of separate low light and high light responses. Planta **213**: 794–801.

Björkman, O. (1981). Responses to Different Quantum Flux Densities. In Physiological Plant Ecology I: Responses to the Physical Environment, O.L. Lange, P.S. Nobel, C.B. Osmond, and H. Ziegler, eds (Springer Berlin Heidelberg: Berlin, Heidelberg), pp. 57–107.

Bjorkman, O. and Holmgren, P. (1963). Adaptability of the Photosynthetic Apparatus to Light Intensity in Ecotypes from Exposed and Shaded Habitats. Physiol. Plant. **16**: 889–914.

Bloom, A.J., Smart, D.R., Nguyen, D.T., and Searles, P.S. (2002). Nitrogen assimilation and growth of wheat under elevated carbon dioxide. Proc. Natl. Acad. Sci. U. S. A. **99**: 1730–1735.

Brooks, M.D. and Niyogi, K.K. (2011). Use of a pulse-amplitude modulated chlorophyll fluorometer to study the efficiency of photosynthesis in Arabidopsis plants. Methods Mol. Biol. **775**: 299–310.

Busch, F.A., Sage, R.F., and Farquhar, G.D. (2018). Plants increase CO2 uptake by assimilating nitrogen via the photorespiratory pathway. Nat Plants **4**: 46–54.

Cao, J. et al. (2011). Whole-genome sequencing of multiple Arabidopsis thaliana populations. Nat. Genet. **43**: 956–963.

Carrier, P., Chagvardieff, P., and Tapie, P. (1989). Comparison of the Oxygen Exchange between Photosynthetic Cell Suspensions and Detached Leaves of Euphorbia characias L. Plant Physiol. **91**: 1075–1079.

Cocuron, J.-C. and Alonso, A.P. (2014). Liquid Chromatography Tandem Mass Spectrometry for Measuring 13C-labeling in Intermediates of the Glycolysis and Pentose Phosphate Pathway. In Plant Metabolic Flux Analysis: Methods and Protocols, M. Dieuaide-Noubhani and A.P. Alonso, eds (Humana Press: Totowa, NJ), pp. 131–142.

Cocuron, J.-C., Anderson, B., Boyd, A., and Alonso, A.P. (2014). Targeted metabolomics of

Physaria fendleri, an industrial crop producing hydroxy fatty acids. Plant Cell Physiol. **55**: 620–633.

Cohu, C.M., Muller, O., Demmig-Adams, B., and Adams, W.W., 3rd (2013). Minor loading vein acclimation for three Arabidopsis thaliana ecotypes in response to growth under different temperature and light regimes. Front. Plant Sci. **4**: 240.

Coschigano, K.T., Melo-Oliveira, R., Lim, J., and Coruzzi, G.M. (1998). Arabidopsis gls mutants and distinct Fd-GOGAT genes. Implications for photorespiration and primary nitrogen assimilation. Plant Cell **10**: 741–752.

Delieu, T. and Walker, D.A. (1981). POLAROGRAPHIC MEASUREMENT OF PHOTOSYNTHETIC OXYGEN EVOLUTION BY LEAF DISCS. New Phytologist **89**: 165–178.

Demmig-Adams, B., Stewart, J.J., and Adams, W.W., 3rd (2017). Environmental regulation of intrinsic photosynthetic capacity: an integrated view. Curr. Opin. Plant Biol. **37**: 34–41.

Demmig-Adams, B., Stewart, J.J., and Adams, W.W., 3rd (2014). Multiple feedbacks between chloroplast and whole plant in the context of plant adaptation and acclimation to the environment. Philos. Trans. R. Soc. Lond. B Biol. Sci. **369**: 20130244.

Demmig-Adams, B., Stewart, J.J., Baker, C.R., and Adams, W.W. (2018). Optimization of Photosynthetic Productivity in Contrasting Environments by Regulons Controlling Plant Form and Function. Int. J. Mol. Sci. **19**.

Dirks, R.C., Singh, M., Potter, G.S., Sobotka, L.G., and Schaefer, J. (2012). Carbon partitioning in soybean (Glycine max) leaves by combined 11C and 13C labeling. New Phytol. **196**: 1109–1121.

Driever, S.M., Lawson, T., Andralojc, P.J., Raines, C.A., and Parry, M.A.J. (2014). Natural variation in photosynthetic capacity, growth, and yield in 64 field-grown wheat genotypes. J. Exp. Bot. **65**: 4959–4973.

Dutilleul, C., Lelarge, C., Prioul, J.-L., De Paepe, R., Foyer, C.H., and Noctor, G. (2005). Mitochondria-driven changes in leaf NAD status exert a crucial influence on the control of nitrate assimilation and the integration of carbon and nitrogen metabolism. Plant Physiol. **139**: 64–78.

Dyson, B.C., Allwood, J.W., Feil, R., Xu, Y.U.N., Miller, M., Bowsher, C.G., Goodacre, R., Lunn, J.E., and Johnson, G.N. (2015). Acclimation of metabolism to light in A rabidopsis thaliana: the glucose 6-phosphate/phosphate translocator GPT 2 directs metabolic acclimation. Plant Cell Environ. **38**: 1404–1417.

Evans, J.R. (1996). Developmental Constraints on Photosynthesis: Effects of Light and Nutrition. In Photosynthesis and the Environment, N.R. Baker, ed (Kluwer Academic Publishers: Netherlands), pp. 281–304.

Evans, J.R., Morgan, P.B., and von Caemmerer, S. (2017). Light Quality Affects Chloroplast Electron Transport Rates Estimated from Chl Fluorescence Measurements. Plant and Cell Physiology **58**: 1652–1660.

Evans, J.R. and Poorter, H. (2001). Photosynthetic acclimation of plants to growth irradiance: the relative importance of specific leaf area and nitrogen partitioning in maximizing carbon gain. Plant Cell Environ. **24**: 755–767.

Figueroa, C.M., Feil, R., Ishihara, H., Watanabe, M., Kölling, K., Krause, U., Höhne, M., Encke, B., Plaxton, W.C., Zeeman, S.C., and Others (2016). Trehalose 6--phosphate coordinates organic and amino acid metabolism with carbon availability. Plant J. **85**: 410–423.

Florian, A., Araújo, W.L., and Fernie, A.R. (2013). New insights into photorespiration obtained from metabolomics. Plant Biol. **15**: 656–666.

Flügel, F., Timm, S., Arrivault, S., Florian, A., Stitt, M., Fernie, A.R., and Bauwe, H. (2017). The Photorespiratory Metabolite 2-Phosphoglycolate Regulates Photosynthesis and Starch Accumulation in Arabidopsis. Plant Cell **29**: 2537–2551.

Foyer, C.H., Noctor, G., Lelandais, M., Lescure, J.C., Valadier, M.H., Boutin, J.P., and Horton, P. (1994). Short-term effects of nitrate, nitrite and ammonium assimilation on photosynthesis, carbon partitioning and protein phosphorylation in maize. Planta **192**: 211–220.

Foyer, C.H., Parry, M., and Noctor, G. (2003). Markers and signals associated with nitrogen assimilation in higher plants. J. Exp. Bot. **54**: 585–593.

Gibon, Y., Blaesing, O.E., Hannemann, J., Carillo, P., Höhne, M., Hendriks, J.H.M., Palacios, N., Cross, J., Selbig, J., and Stitt, M. (2004). A robot-based platform to measure multiple enzyme activities in Arabidopsis using a set of cycling assays: comparison of changes of enzyme activities and transcript levels during diurnal cycles and in prolonged darkness. Plant Cell **16**: 3304–3325.

Givnish, T.J. (1988). Adaptation to Sun and Shade: a Whole-Plant Perspective. Funct. Plant Biol. **15**: 63–92.

Goldschmidt, E.E. and Huber, S.C. (1992). Regulation of photosynthesis by end-product accumulation in leaves of plants storing starch, sucrose, and hexose sugars. Plant Physiol. **99**: 1443–1448.

Hald, S., Nandha, B., Gallois, P., and Johnson, G.N. (2008). Feedback regulation of photosynthetic electron transport by NADP(H) redox poise. Biochim. Biophys. Acta **1777**: 433–440.

Hanson, H.C. (1917). Leaf-Structure as Related to Environment. Am. J. Bot. **4**: 533–560.

Häusler, R.E., Heinrichs, L., Schmitz, J., and Flügge, U.-I. (2014). How sugars might coordinate chloroplast and nuclear gene expression during acclimation to high light intensities. Mol. Plant **7**: 1121–1137.

Herrmann, H.A., Schwartz, J.-M., and Johnson, G.N. (2019). Metabolic acclimation—a key to enhancing photosynthesis in changing environments? J. Exp. Bot. **70**: 3043–3056.

Huner, N., Dahal, K., Hollis, L., Bode, R., Rosso, D., Krol, M., and Ivanov, A. (2012). Chloroplast redox imbalance governs phenotypic plasticity: the “grand design of

photosynthesis" revisited. Front. Plant Sci. **3**: 255.

Huppe, H.C. and Turpin, D.H. (1994). Integration of Carbon and Nitrogen Metabolism in Plant and Algal Cells. Annu. Rev. Plant Physiol. Plant Mol. Biol. **45**: 577–607.

Keeley, J.E. and Rundel, P.W. (2003). Evolution of CAM and C4 Carbon-Concentrating Mechanisms. Int. J. Plant Sci. **164**: S55–S77.

Kramer, D.M., Johnson, G., Kiirats, O., and Edwards, G.E. (2004). New Fluorescence Parameters for the Determination of QA Redox State and Excitation Energy Fluxes. Photosynth. Res. **79**: 209.

Leegood, R.C., Lea, P.J., Adcock, M.D., and Häusler, R.E. (1995). The regulation and control of photorespiration. J. Exp. Bot. **46**: 1397–1414.

Li, J., Weraduwage, S.M., Preiser, A.L., Tietz, S., Weise, S.E., Strand, D.D., Froehlich, J.E., Kramer, D.M., Hu, J., and Sharkey, T.D. (2019). A Cytosolic Bypass and G6P Shunt in Plants Lacking Peroxisomal Hydroxypyruvate Reductase. Plant Physiol. **180**: 783–792.

Li, Z., Wakao, S., Fischer, B.B., and Niyogi, K.K. (2009). Sensing and responding to excess light. Annu. Rev. Plant Biol. **60**: 239–260.

Long, S.P. and Bernacchi, C.J. (2003). Gas exchange measurements, what can they tell us about the underlying limitations to photosynthesis? Procedures and sources of error. J. Exp. Bot. **54**: 2393–2401.

Long, S.P., Marshall-Colon, A., and Zhu, X.-G. (2015). Meeting the global food demand of the future by engineering crop photosynthesis and yield potential. Cell **161**: 56–66.

Loreto, F., Tsonev, T., and Centritto, M. (2009). The impact of blue light on leaf mesophyll conductance. J. Exp. Bot. **60**: 2283–2290.

Ma, F., Jazmin, L.J., Young, J.D., and Allen, D.K. (2014). Isotopically nonstationary 13C flux analysis of changes in Arabidopsis thaliana leaf metabolism due to high light acclimation. Proc. Natl. Acad. Sci. U. S. A. **111**: 16967–16972.

McClain, A.M. and Sharkey, T.D. (2020). Building a better equation for electron transport estimated from Chl fluorescence: accounting for nonphotosynthetic light absorption. New Phytol. **225**: 604–608.

Mekala, N.R., Suorsa, M., Rantala, M., Aro, E.-M., and Tikkanen, M. (2015). Plants Actively Avoid State Transitions upon Changes in Light Intensity: Role of Light-Harvesting Complex II Protein Dephosphorylation in High Light. Plant Physiol. **168**: 721–734.

Murchie, E.H. and Horton, P. (1997). Acclimation of photosynthesis to irradiance and spectral quality in British plant species: chlorophyll content, photosynthetic capacity and habitat preference. Plant Cell Environ. **20**: 438–448.

Nunes-Nesi, A., Fernie, A.R., and Stitt, M. (2010). Metabolic and signaling aspects underpinning the regulation of plant carbon nitrogen interactions. Mol. Plant **3**: 973–996.

Osmond, B., Badger, M., Maxwell, K., Björkman, O., and Leegood, R. (1997). Too many photons: photorespiration, photoinhibition and photooxidation. Trends Plant Sci. **2**:

119–121.

Pammenter, N.W., Loreto, F., and Sharkey, T.D. (1993). End product feedback effects on photosynthetic electron transport. Photosynth. Res. **35**: 5–14.

Park, Y.-I., Chow, W.S., Barry Osmond, C., and Anderson, J.M. (1996). Electron transport to oxygen mitigates against the photoinactivation of Photosystem II in vivo. Photosynthesis Research **50**: 23–32.

Parry, M.A.J., Reynolds, M., Salvucci, M.E., Raines, C., Andralojc, P.J., Zhu, X.-G., Price, G.D., Condon, A.G., and Furbank, R.T. (2011). Raising yield potential of wheat. II. Increasing photosynthetic capacity and efficiency. J. Exp. Bot. **62**: 453–467.

Paul, M. (2007). Trehalose 6-phosphate. Curr. Opin. Plant Biol. **10**: 303–309.

Paul, M.J. and Pellny, T.K. (2003). Carbon metabolite feedback regulation of leaf photosynthesis and development. J. Exp. Bot. **54**: 539–547.

Plaxton, W. and McManus, M.T. (2006). Annual Plant Reviews, Control of Primary Metabolism in Plants (John Wiley & Sons).

Pracharoenwattana, I., Zhou, W., Keech, O., Francisco, P.B., Udomchalothorn, T., Tschoep, H., Stitt, M., Gibon, Y., and Smith, S.M. (2010). Arabidopsis has a cytosolic fumarase required for the massive allocation of photosynthate into fumaric acid and for rapid plant growth on high nitrogen. Plant J. **62**: 785–795.

Rachmilevitch, S., Cousins, A.B., and Bloom, A.J. (2004). Nitrate assimilation in plant shoots depends on photorespiration. Proc. Natl. Acad. Sci. U. S. A. **101**: 11506–11510.

Ritchie, R.J. (2006). Consistent sets of spectrophotometric chlorophyll equations for acetone, methanol and ethanol solvents. Photosynth. Res. **89**: 27–41.

Ritchie, R.J. (2008). Universal chlorophyll equations for estimating chlorophylls a, b, c, and d and total chlorophylls in natural assemblages of photosynthetic organisms using acetone, methanol, or ethanol solvents. Photosynthetica **46**: 115–126.

Savitch, L.V., Massacci, A., Gray, G.R., and Huner, N.P.A. (2000). Acclimation to low temperature or high light mitigates sensitivity to photoinhibition: roles of the Calvin cycle and the Mehler reaction. Funct. Plant Biol. **27**: 253–264.

von Schaewen, A., Stitt, M., Schmidt, R., Sonnewald, U., and Willmitzer, L. (1990). Expression of a yeast-derived invertase in the cell wall of tobacco and Arabidopsis plants leads to accumulation of carbohydrate and inhibition of photosynthesis and strongly influences growth and phenotype of transgenic tobacco plants. EMBO J. **9**: 3033–3044.

Sharkey, T.D. (1988). Estimating the rate of photorespiration in leaves. Physiologia Plantarum **73**: 147–152.

Somerville, C.R. and Ogren, W.L. (1980). Arabidopsis mutants, which do not have a ferredoxin glutamate synthase. Nature **286**: 257–259.

Somerville, C.R. and Ogren, W.L. (1982). Mutants of the cruciferous plant Arabidopsis thaliana lacking glycine decarboxylase activity. Biochem. J **202**: 373–380.

Somerville, C.R. and Ogren, W.L. (1981). Photorespiration-deficient Mutants of Arabidopsis thaliana Lacking Mitochondrial Serine Transhydroxymethylase Activity. Plant Physiol. **67**: 666–671.

South, P.F., Cavanagh, A.P., Liu, H.W., and Ort, D.R. (2019). Synthetic glycolate metabolism pathways stimulate crop growth and productivity in the field. Science **363**.

Stewart, J.J., Polutchko, S.K., Adams, W.W., 3rd, and Demmig-Adams, B. (2017). Acclimation of Swedish and Italian ecotypes of Arabidopsis thaliana to light intensity. Photosynth. Res. **134**: 215–229.

Strand, Å., Hurry, V., Henkes, S., Huner, N., Gustafsson, P., Gardeström, P., and Stitt, M. (1999). Acclimation of Arabidopsis Leaves Developing at Low Temperatures. Increasing Cytoplasmic Volume Accompanies Increased Activities of Enzymes in the Calvin Cycle and in the Sucrose-Biosynthesis Pathway. Plant Physiology **119**: 1387–1398.

Strand, D.D. (2014). Redox regulation of cyclic electron flow around photosystem I.

Timm, S., Florian, A., Arrivault, S., Stitt, M., Fernie, A.R., and Bauwe, H. (2012). Glycine decarboxylase controls photosynthesis and plant growth. FEBS Lett. **586**: 3692–3697.

Timm, S., Florian, A., Fernie, A.R., and Bauwe, H. (2016). The regulatory interplay between photorespiration and photosynthesis. J. Exp. Bot. **67**: 2923–2929.

Timm, S., Woitschach, F., Heise, C., Hagemann, M., and Bauwe, H. (2019). Faster Removal of 2-Phosphoglycolate through Photorespiration Improves Abiotic Stress Tolerance of Arabidopsis. Plants **8**: 563.

Walters, R.G., Shephard, F., Rogers, J.J.M., Rolfe, S.A., and Horton, P. (2003). Identification of mutants of Arabidopsis defective in acclimation of photosynthesis to the light environment. Plant Physiol. **131**: 472–481.

Wingler, A., Lea, P.J., Quick, W.P., and Leegood, R.C. (2000). Photorespiration: metabolic pathways and their role in stress protection. Philos. Trans. R. Soc. Lond. B Biol. Sci. **355**: 1517–1529.

Tables

Table 1. Results of regression analysis for parameters in Figures 7, S7, and S8.

	Fold Change (HL/LL)		*HL*		*LL*	
Parameter	ETR_{max}	P_{max}	ETR_{max}	P_{max}	ETR_{max}	P_{max}
Gln/Glu	***	**	**	*n.s.*	**	*
Gln + Glu *(nmol mg DW^{-1})*	*n.s.*	*n.s.*	*n.s.*	*n.s.*	*n.s.*	*n.s.*
Gly/Ser	**	*	**	*n.s.*	*	*n.s.*
Gly + Ser *(nmol mg DW^{-1})*	**	*n.s.*	*n.s.*	*n.s.*	*	*n.s.*
GS *(mmol ADP min^{-1} mg $protein^{-1}$)*	**	*n.s.*	*n.s.*	*n.s.*	**	*n.s.*
Fd-GOGAT *(mmol glutamate min^{-1} mg $protein^{-1}$)*	*n.s.*	*	*n.s.*	*n.s.*	*n.s.*	*n.s.*

Significant correlations are denoted by asterisks; * = $R^2 > 0.05$, ** = $R^2 > 0.1$, *** = $R^2 > 0.5$ (*n.s.* = not significant). denotes an inverse correlation.

Figure Legends

Figure 1. The dynamics of photosynthetic capacity acclimation to HL in the Col-0, IT, and SW ecotypes. (a) Photosynthetic capacity as measured by maximum electron transport rate, ETR_{max} (i.e., maximal light-saturated photosynthetic electron transport rate) per leaf area (green), maximum oxygen evolution rate, P_{max} (i.e., maximal CO_2- and light-saturated oxygen evolution rate) rate per area (blue), and P_{max} per unit dry leaf mass (DW^{-1}) (purple). Q_A redox state was measured as q_L (orange). Mean values combine data from Col-0, IT, and SW ecotypes ± standard errors (n = 12). (b) ETR_{max} per unit area, (c) P_{max} per unit area, and (d) P_{max} per DW^{-1} for the Col-0, IT, and SW plotted individually. Mean values ± standard errors (n = 4) are given an asterisk if the mean value at the indicated time point was significantly different from the mean value for that ecotype at Day 0 based on a one-way ANOVA and post hoc Tukey–Kramer HSD tests.

Figure 2. Natural diversity in photosynthetic capacity acclimation response to HL. (a) Photosynthetic capacity as measured by ETR_{max} and P_{max} per leaf area for Col-0, IT, SW, and the ecotype panel (Cao et al., 2011) plants from LL growth (LL) and on HL Day 4 (HL). LL and HL plants are displayed on a shared color-scale for ETR_{max} and P_{max}, respectively, from low (dark blue) to high (carmine red). Fold-change (HL/LL) values are shown on a separate color scale with a range of 0.5 (cyan) to 2.25 (magenta). Each ecotype is assigned a unique number in descending order of the magnitude of the HL/LL ETR_{max} fold-change. (b-d) Correlation of P_{max} with $ETR_{max}/4$ data for (b) HL/LL fold-change, (c) HL plants, and (d) LL plants. Best-fit regression and associated R^2-values (black) and theoretical 1:1 regression (magenta) are displayed. Ecotype numbers corresponding to the unique number for each ecotype in panel a (red) are included for the outlier ecotypes. ETR_{max} and P_{max} mean values were calculated using n = 2 to 4 biological replicates.

Figure 3. Leaf metabolomic data for metabolite classes and selected individual metabolites. Abundance of total soluble sugars, sugar phosphates, organic acids, and amino acids (AAs) classes displayed alongside selected metabolites (metabolites with a HL/LL abundance change) from each class for Col-0 (no outside square) and SW (black squares). The abundance of the

metabolite for LL-grown and HL-shifted plants are displayed on a shared color-scale, low (dark blue) to high (carmine red). Log_2-transformed HL/LL fold changes are displayed on a separate color scale from -3 (cyan) to +3 (magenta). Mean values are calculated from n = 3 to 8 biological replicates.

Figure 4. Metabolites most strongly linked to HL acclimation in the SW and Col-0 ecotypes. Variable importance in projection (VIP) scores showing the highest 20 metabolites that contribute the most to the separation for (a) SW and (b) Col-0 plants. Relative metabolite abundance in LL and HL plants are displayed on a color scale; high abundance (carmine red) and low abundance (dark blue).

Figure 5. Correlation of change in metabolite abundance with photosynthetic capacity. Correlation coefficients of time-resolved metabolomics data in HL-shifted SW plants with the change in ETR_{max} per unit area, P_{max} per unit area, and A_{max} per unit area at the same sampling points; positive correlations (red) and negative correlations (blue).

Figure 6. Low oxygen suppresses the HL-dependent increase in Gln/Glu and Gly/Ser. Metabolite quantification of the (a) Gln/Glu ratio, (b) nmol Gln + Glu per mg dry leaf weight (DW), (c) Gly/Ser ratio, and (d) nmol Gly + Ser per mg DW^{-1} for Col-0 (purple), IT (green), and SW (orange) plants are grown in LL and HL Day 1 and Day 3 in ambient air or Day 3 post-HL shift in low oxygen air (400 ppm CO_2, 2% O_2, balance N_2). Mean values ± standard errors (n = 3 to 8) with individual data points displayed as dots (black). Mean values that share the same letters are not statistically different, and those that do not share the same letters are statistically different based on one-way ANOVA and post hoc Tukey–Kramer HSD tests.

Figure 7. Correlation of metabolic indicators of photorespiration and nitrogen assimilation rates on HL Day 1 with increased photosynthetic capacity on HL Day 4. Fold-change (HL/LL) of ETR_{max} per leaf area for Col-0, IT, SW, and the ecotype panel(Cao et al., 2011) with quantification of (a) Gln/Glu, (b) Gly/ser, (c) nmol Ser + Gly per mg DW^{-1}, and (d) glutamine synthetase (GS) activity (mmol adenosine diphosphate (ADP) min^{-1} mg $protein^{-1}$) levels on HL Day 1. ETR_{max} mean values were calculated using n = 2 to 4 biological replicates. Metabolite and

enzymatic rate quantifications were calculated using n = 2 to 4 biological replicates and n = 2 technical replicates for each biological replicate. Ecotype numbers (red) correspond to numbers in Fig. 2A.

Figure 8. Low oxygen air enables photosynthetic capacity acclimation in HL in ecotypes with weak responses in ambient oxygen conditions. (a) Photosynthetic capacity as measured by P_{max} per leaf area for Col-0, IT, SW, and a subset of ecotypes selected from the larger ecotype panel(Cao et al., 2011) to capture the full phenotypic range of photosynthetic capacity acclimation responses were assayed at HL Day 4 (HL) in ambient O_2 air, in low O_2 air (400 ppm CO_2, 2% O_2, balance nitrogen), and in high O_2 air (400 ppm CO_2, 30% O_2, balance nitrogen). Mean values for individual ecotypes are shown as black circles for n = 3 biological replicates. (b) P_{max} at HL Day 4 and 7 in ambient O_2 air, low O_2 air, and high O_2 air measured in Col-0 (purple), IT (green), SW (orange) ecotype, and two photorespiration mutants (serine-hydroxymethyltransferase 1 (*shm1*) and Fd-dependent glutamine-oxoglutarate glutamate aminotransferase 1-30 (*gls1-30*)), which were generated in the Col-0 background. Mean values ± standard errors (n = 3). Mean values that share the same letters are not statistically different, and those that do not share the same letters are statistically different based on one-way ANOVA and post hoc Tukey–Kramer HSD tests. Values for conditions where plants wilted and showed signs of chlorosis were not determined (ND).

Figure 9. Model of the control of photosynthetic capacity acclimation by nitrogen assimilation and photorespiration pathways. The left side presents the situation for an ecotype with strong photosynthetic capacity acclimation to HL. Rapid utilization of end-products of PET in the chloroplast via pathways including N assimilation and photorespiration maintains an oxidized Q_A state, limiting feedback inhibition and licensing photosynthetic capacity acclimation to HL. The right side presents the situation for an ecotype with weak photosynthetic capacity acclimation to HL. Limited photorespiratory capacity represses the utilization of products of PET, in turn repressing PET rates.

Supplemental Materials

Supplemental Figure Legends

Figure S1. Determining conditions necessary for saturating light and CO_2 to measure photosynthetic capacity and metabolic pathway depictions. (a) Simple cartoon of nitrogen assimilation in the chloroplast in plants. (b) Simple cartoon of glycine decarboxylase (GDC) activity in the mitochondria within the photorespiration pathway. (c-f) SW ecotype plants grown in LL (grey) or Day 10 after shift to HL (black) assayed for (c) ΦPS_{II}, (d) electron transport rate (μmol e^- m^{-2} s^{-1}), and (e) O_2 evolution rate (μmol e^- m^{-2} s^{-1}) over a range of photon flux densities (PFD, μmol quanta m^{-2} s^{-1}), and (f) CO_2 net assimilation rate at saturating light over a range of intracellular CO_2 concentrations (C_i, μmol CO_2 mol^{-1} air).

Figure S2. The dynamics of photosynthetic capacity acclimation to HL in the Col-0, IT, and SW ecotypes. (a-d) Photosynthetic capacity as measured by (a) maximum electron transport rate, ETR_{max} (i.e., maximal light-saturated photosynthetic electron transport rate) per leaf area, (b) maximum oxygen evolution rate, P_{max} (i.e., maximal CO_2- and light-saturated oxygen evolution rate) rate per area, (c) maximum carbon assimilation rate, A_{max} (i.e., maximal CO_2- and light-saturated CO_2 assimilation rate) per leaf area, and (d) P_{max} per unit dry leaf mass. (e) Q_A redox state as measured by q_L at growth light intensity. Col-0 (purple), IT (green), and SW (orange) plants that were grown in either low light (LL) or shifted to high-light (HL) at measurement Day 0. Mean values ± standard errors (n = 4) with individual data points displayed as dots (black). Mean values that share the same letters are not considered statistically different and those that do not share the same letters are considered statistically different based on one-way ANOVA and post hoc Tukey–Kramer HSD tests.

Figure S3. The response of chlorophyll per unit area to HL shift. (a) Ratio of chlorophyll per unit area in Day 4 HL-shifted (HL) over LL-grown (LL) plants for Col-0, IT, SW, and the ecotype panel(Cao et al., 2011). Mean values are calculated using n = 2 to 4. Scatter plots of fold change in chlorophyll per unit area (HL/LL) plotted against the fold change in photosynthetic

capacity (HL/LL) as measured by (b) ETR_{max} and (c) P_{max} for the same plants as those used to quantify chlorophyll per unit area.

Figure S4. Natural diversity in Q_A redox state in response to a HL shift measured under saturating light. Correlation of Q_A redox state as measured by q_L with photosynthetic capacity as measured by ETR_{max} for Col-0, IT, SW, and the ecotype panel(Cao et al., 2011). (a) q_L and ETR_{max} assayed in LL-grown plants, (b) q_L and ETR_{max} assayed in Day 4 HL-shifted plants (HL), and (c) fold change (HL/LL) for q_L and ETR_{max}. Best-fit regression and associated R^2-values (black) and theoretical 1:1 regression (magenta) are displayed. Ecotype numbers (red) corresponding to the unique number for each ecotype Fig. 2A. ETR_{max} and q_L mean values were calculated using n = 2 to 4.

Figure S5. Differentiation of metabolomes by ecotype, growth condition, and time component. Unsupervised principal component analysis (PCA) of metabolomic data from LL plants (green) and HL-shifted plants (pink) for the (a) SW and (b) Col-0 ecotypes. The shaded regions in the PCA plots represent 95% confidence intervals. Unsupervised PCAs of metabolomic data for (c) SW LL (cyan), Col-0 LL (green), SW post-HL shift Day 1 (blue), and Col-0 post-HL Day 1 (red) plants, and (c) SW plants post-HL shift Day 10 (cyan), HL Day 6 (blue), HL Day 3 (green), HL Day 1 (red), LL grown plant Day 10 (orange), LL Day 6 (yellow), LL grown Day 3 (dark purple), and LL grown Day 1 (fuchsia).

Figure S6. Response of gas exchange parameters related to photorespiration after the HL shift in Col-0, IT, and SW ecotypes (a) Stomatal conductance (mol H_20 m^{-2} s^{-1}) measured under growth conditions, (b) O_2 inhibition of net photosynthetic rate (P_n) measured at saturating light, and (c) post-illumination CO_2 burst (PIB) quantified as maximum respiration rate (µmol CO_2 m^{-2} s^{-1}) in the dark averaged over 10 seconds after 20 min of saturating light. Col-0 (purple), IT (green), and SW (orange) plants were grown in either low light (LL) or shifted to high-light (HL) at measurement Day 0. Mean values ± standard errors (n = 4).

Figure S7. Correlation of metabolic indicators of photorespiration and nitrogen assimilation rates on HL Day 1 with increased photosynthetic capacity on HL Day 4 as

measured P_{max}. Correlation of Col-0, IT, SW, and the ecotype panel(Cao et al., 2011) for (a-c) fold change (HL/LL) in P_{max} in Day 4 post HL-shift (HL) over LL-grown (LL) plants with (a) Gln/Glu ratio, (b) Gly/Ser ratio and (c) Fd-GOGAT (mmol Glu min^{-1} mg $protein^{-1}$) on Day 1 of the post-HL shift. (d) Anticorrelation of P_{max} in LL grown plants with Gln/Glu on Day 1 after HL shift. (e) Correlation of P_{max} in LL grown plants with Gly/Ser ratio on Day 1 after HL shift. P_{max} mean values were calculated using n = 2 to 4. Enzymatic rate quantifications were calculated using n = 2 to 4 biological replicates and n = 2 technical replicates of each biological replicate. Ecotype numbers (red) that correspond to unique numbers in Fig. 2A are included.

Figure S8. Correlation of metabolic indicators of photorespiration and nitrogen assimilation rates on HL Day 1 with increased photosynthetic capacity on HL Day 4 as measured by ETR_{max}. Photosynthetic capacity as measured by ETR_{max} measured in (a) Day 4 after HL shift and (b-d) LL-grown plants for Col-0, IT, SW, and the ecotype panel(Cao et al., 2011) correlated with quantification of (a) Gln/Glu ratio and anticorrelated with (b) Gln/Glu ratio, (c) Gly + Ser (nmol mg DW^{-1}), and (d) GS activity (mmol ADP min^{-1} mg $protein^{-1}$) on Day 1 after HL shift. ETR_{max} mean values were calculated using n = 2 to 4. Enzymatic rates were calculated using n = 2 to 4 biological replicates and n = 2 technical replicates of each biological replicate. Ecotype numbers (red) that correspond to unique numbers in Fig. 2A are included.

Figure S9. Correlation of metabolic indicators of photorespiration and nitrogen assimilation rates on HL Day 1 Q_A redox on HL Day 4 as measured in saturating light. Fold change (HL/LL) of the Q_A redox state as measured by q_L for Col-0, IT, SW, and the ecotype panel(Cao et al., 2011) correlated with quantification of (a) GS activity (mmol ADP min^{-1} mg $protein^{-1}$), (b) Fd-GOGAT activity (mmol Glu min^{-1} mg $protein^{-1}$) on Day 1 of the post-HL shift. (c) q_L from LL-grown plants anticorrelated with GS activity (mmol ADP min^{-1} mg $protein^{-1}$) on Day 1 after HL shift. q_L mean values were calculated using n = 2 to 4. Enzymatic rate quantifications were calculated using n = 2 to 4 biological replicates and n = 2 technical replicates of each biological replicate.

Supplemental Tables

Table S1. Photosynthetic capacity values as measured in P_{max} and ETR_{max} and Q_A redox state as quantified by q_L.

Table S2. LC-MS/MS metabolomics data for all conditions.

Table S3. Gln, Glu, Ser, Gly, GS activity, and Fd-GOGAT activity levels in Col-0, IT, SW, and the ecotype panel from Day 1 after HL shift.

Figure 1

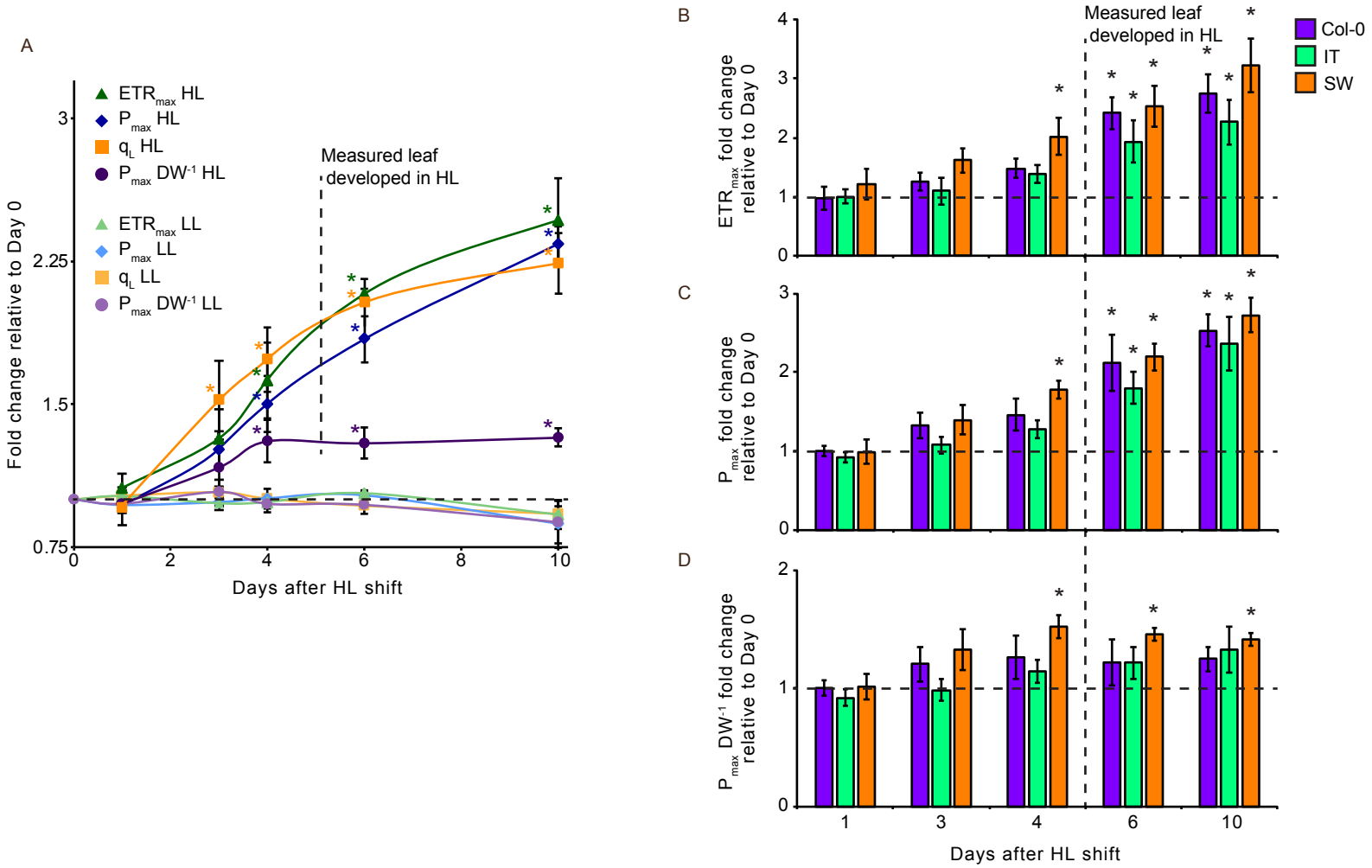
A
ETRmax HL
Pmax HL
qL HL
Pmax DW-1 HL
ETRmax LL
Pmax LL
qL LL
Pmax DW-1 LL
Measured leaf developed in HL
Fold change relative to Day 0
Days after HL shift
B
ETRmax fold change relative to Day 0
Measured leaf developed in HL
Col-0
IT
SW
C
Pmax fold change relative to Day 0
D
Pmax DW-1 fold change relative to Day 0
Days after HL shift

Figure 2

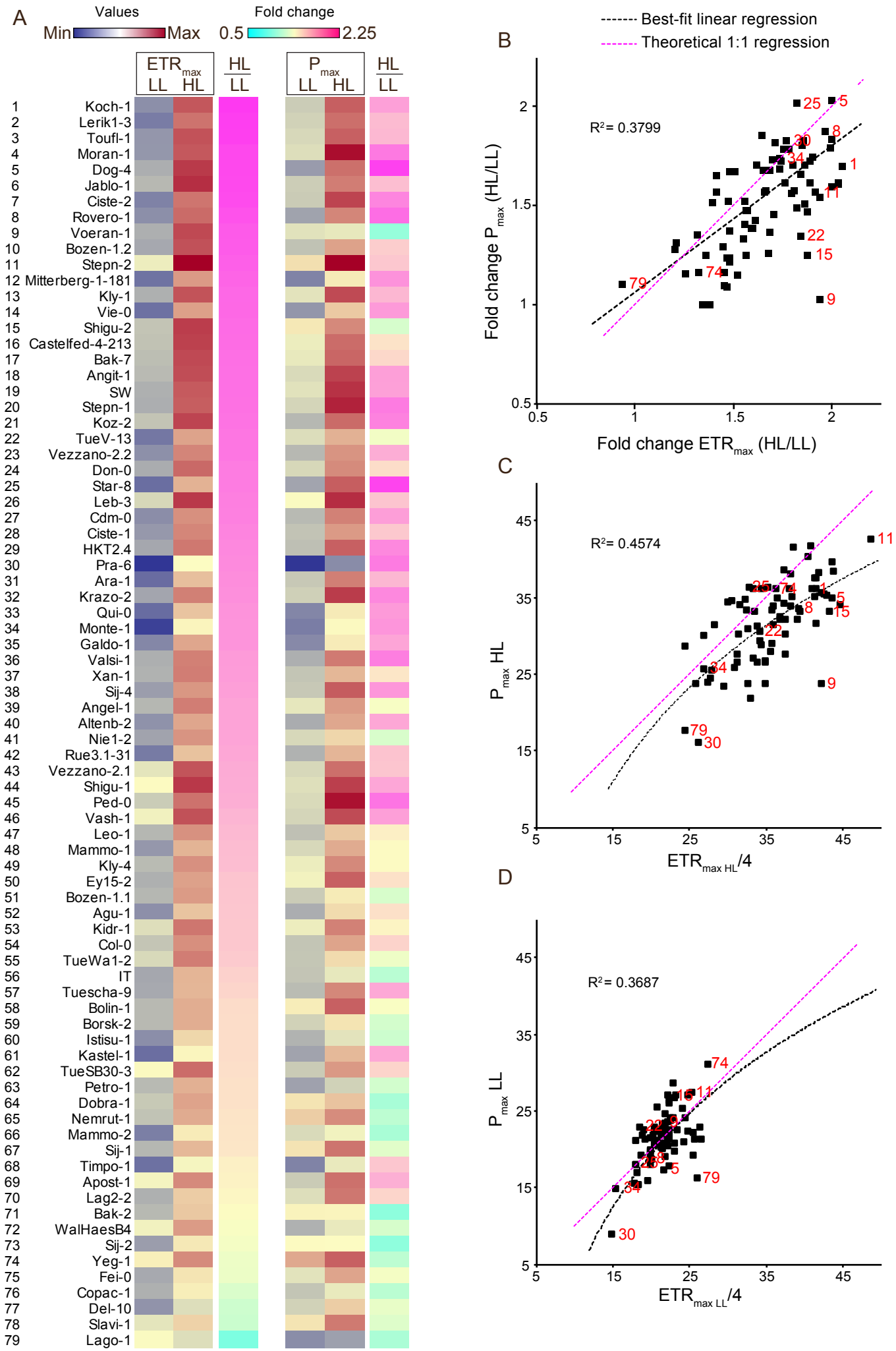
A
Values
Min
Max
Fold change
0.5
2.25
ETRmax
LL
HL
HL/LL
Pmax
LL
HL
HL/LL
1 Koch-1
2 Lerik1-3
3 Toufl-1
4 Moran-1
5 Dog-4
6 Jablo-1
7 Ciste-2
8 Rovero-1
9 Voeran-1
10 Bozen-1.2
11 Stepn-2
12 Mitterberg-1-181
13 Kly-1
14 Vie-0
15 Shigu-2
16 Castelfed-4-213
17 Bak-7
18 Angit-1
19 SW
20 Stepn-1
21 Koz-2
22 TueV-13
23 Vezzano-2.2
24 Don-0
25 Star-8
26 Leb-3
27 Cdm-0
28 Ciste-1
29 HKT2.4
30 Pra-6
31 Ara-1
32 Krazo-2
33 Qui-0
34 Monte-1
35 Galdo-1
36 Valsi-1
37 Xan-1
38 Sij-4
39 Angel-1
40 Altenb-2
41 Nie1-2
42 Rue3.1-31
43 Vezzano-2.1
44 Shigu-1
45 Ped-0
46 Vash-1
47 Leo-1
48 Mammo-1
49 Kly-4
50 Ey15-2
51 Bozen-1.1
52 Agu-1
53 Kidr-1
54 Col-0
55 TueWa1-2
56 IT
57 Tuescha-9
58 Bolin-1
59 Borsk-2
60 Istisu-1
61 Kastel-1
62 TueSB30-3
63 Petro-1
64 Dobra-1
65 Nemrut-1
66 Mammo-2
67 Sij-1
68 Timpo-1
69 Apost-1
70 Lag2-2
71 Bak-2
72 WalHaesB4
73 Sij-2
74 Yeg-1
75 Fei-0
76 Copac-1
77 Del-10
78 Slavi-1
79 Lago-1
B
Best-fit linear regression
Theoretical 1:1 regression
R²= 0.3799
Fold change Pmax (HL/LL)
Fold change ETRmax (HL/LL)
C
R²= 0.4574
Pmax HL
ETRmax HL/4
D
R²= 0.3687
Pmax LL
ETRmax LL/4

Figure 3

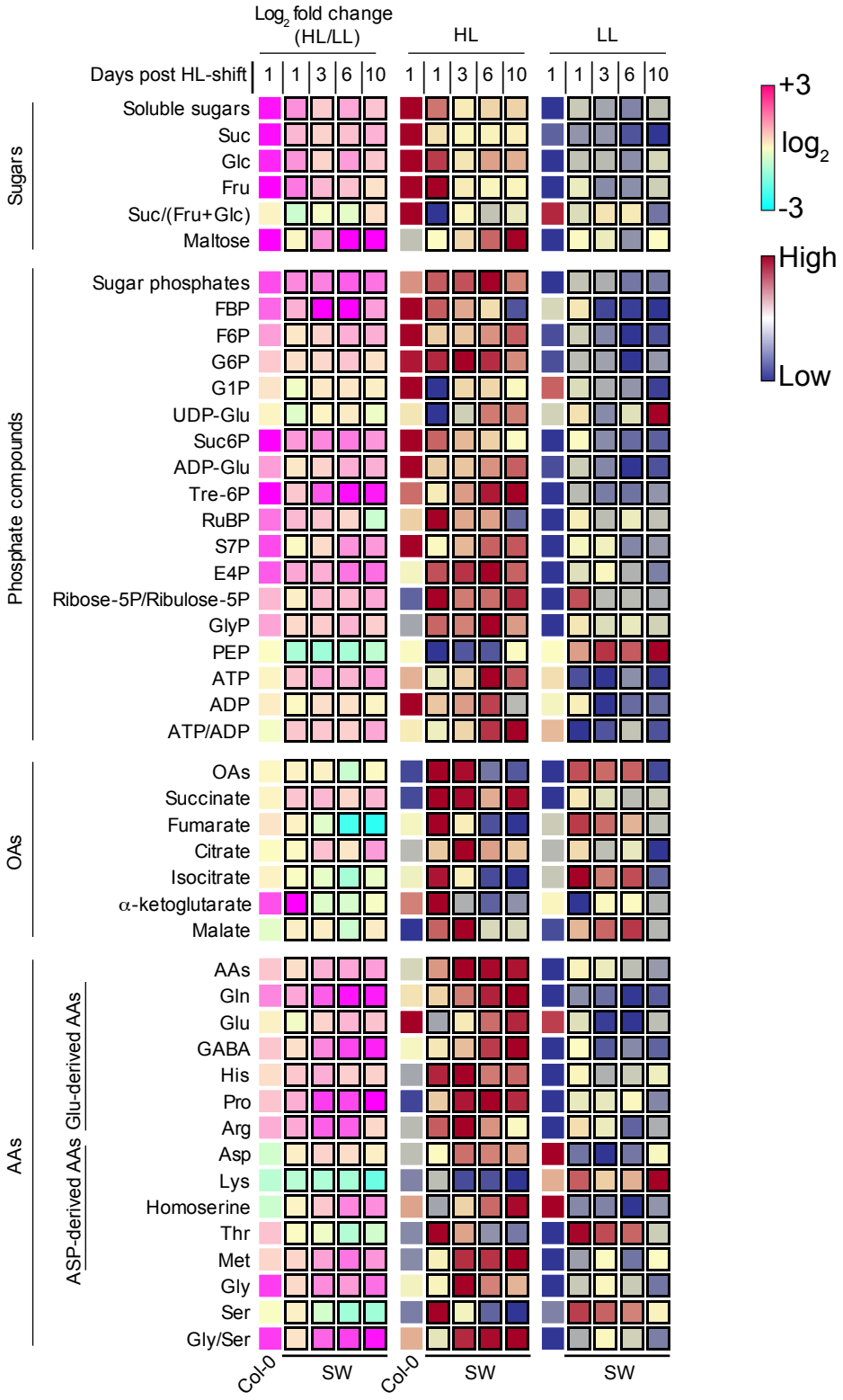
Log2 fold change (HL/LL)
HL
LL
Days post HL-shift
1 1 3 6 10
Sugars
Soluble sugars
Suc
Glc
Fru
Suc/(Fru+Glc)
Maltose
Phosphate compounds
Sugar phosphates
FBP
F6P
G6P
G1P
UDP-Glu
Suc6P
ADP-Glu
Tre-6P
RuBP
S7P
E4P
Ribose-5P/Ribulose-5P
GlyP
PEP
ATP
ADP
ATP/ADP
OAs
OAs
Succinate
Fumarate
Citrate
Isocitrate
α-ketoglutarate
Malate
AAs
AAs
Gln
Glu
GABA
His
Pro
Arg
Asp
Lys
Homoserine
Thr
Met
Gly
Ser
Gly/Ser
Glu-derived AAs
ASP-derived AAs
Col-0
SW
+3
log2
-3
High
Low

Figure 4

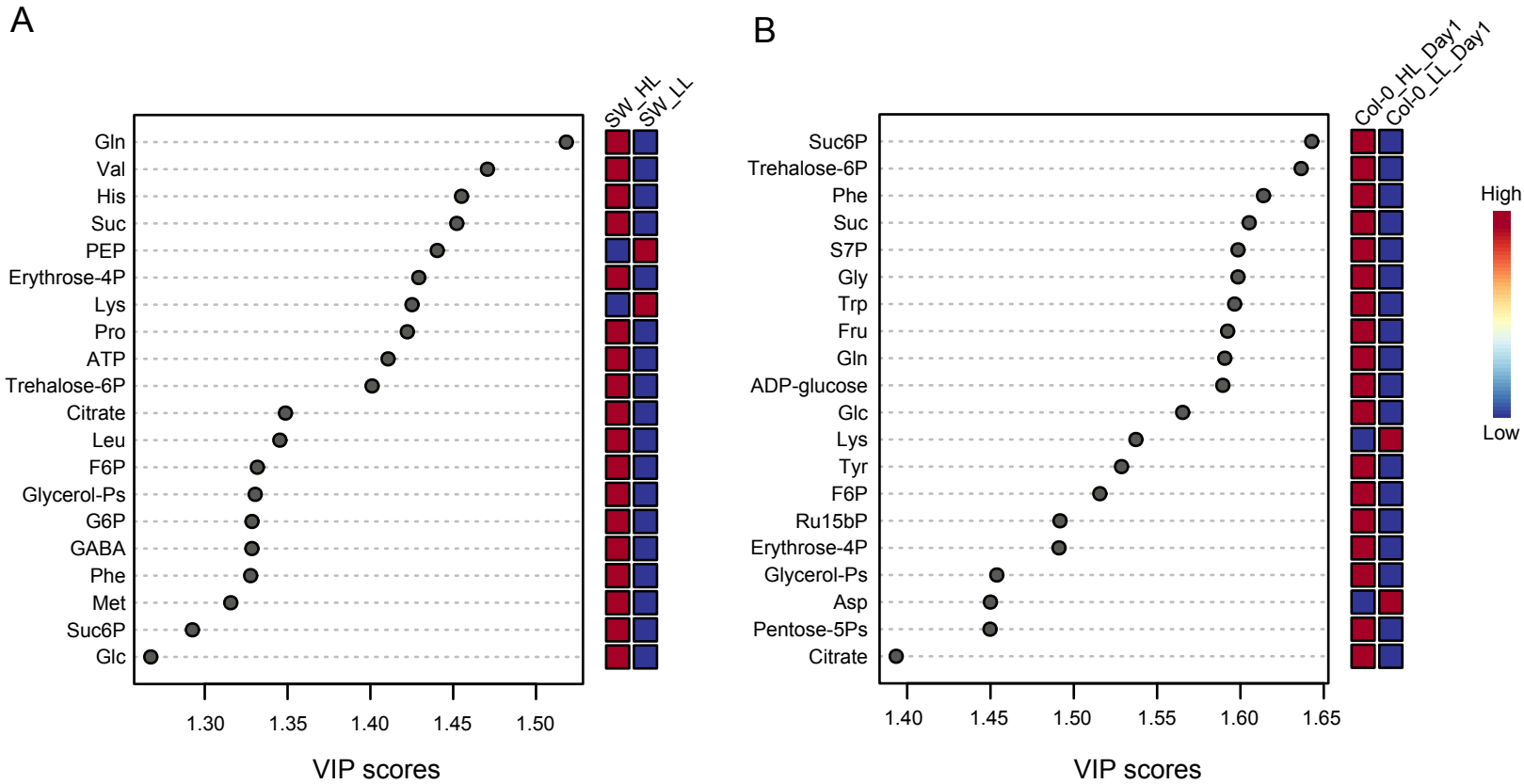
A
SW_HL
SW_LL
Gln
Val
His
Suc
PEP
Erythrose-4P
Lys
Pro
ATP
Trehalose-6P
Citrate
Leu
F6P
Glycerol-Ps
G6P
GABA
Phe
Met
Suc6P
Glc
1.30
1.35
1.40
1.45
1.50
VIP scores
B
Col-0_HL_Day1
Col-0_LL_Day1
Suc6P
Trehalose-6P
Phe
Suc
S7P
Gly
Trp
Fru
Gln
ADP-glucose
Glc
Lys
Tyr
F6P
Ru15bP
Erythrose-4P
Glycerol-Ps
Asp
Pentose-5Ps
Citrate
1.40
1.45
1.50
1.55
1.60
1.65
VIP scores
High
Low

Figure 5

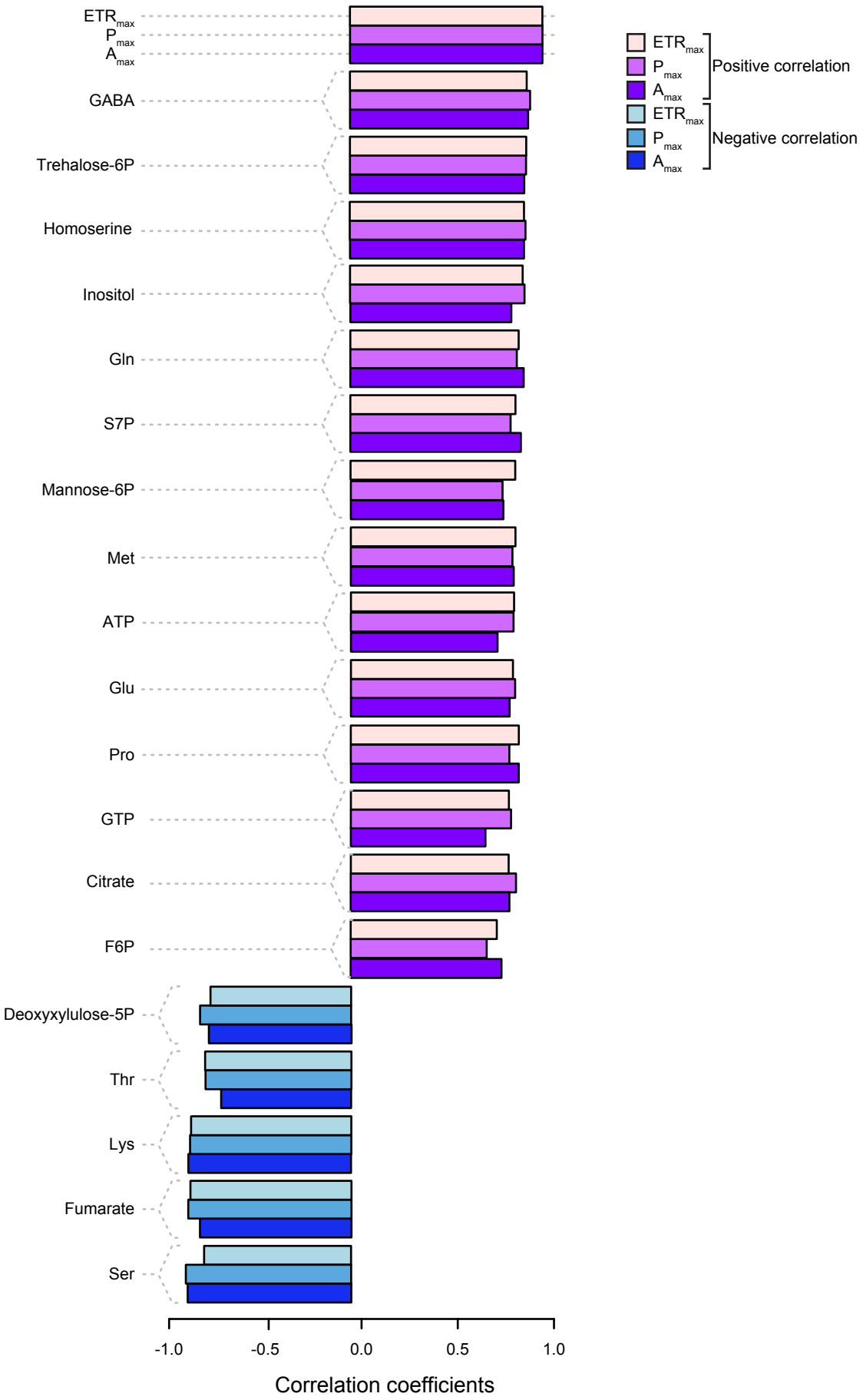
ETRmax
Pmax
Amax
GABA
Trehalose-6P
Homoserine
Inositol
Gln
S7P
Mannose-6P
Met
ATP
Glu
Pro
GTP
Citrate
F6P
Deoxyxylulose-5P
Thr
Lys
Fumarate
Ser
-1.0
-0.5
0.0
0.5
1.0
Correlation coefficients
ETRmax
Pmax
Amax
Positive correlation
ETRmax
Pmax
Amax
Negative correlation

Figure 6

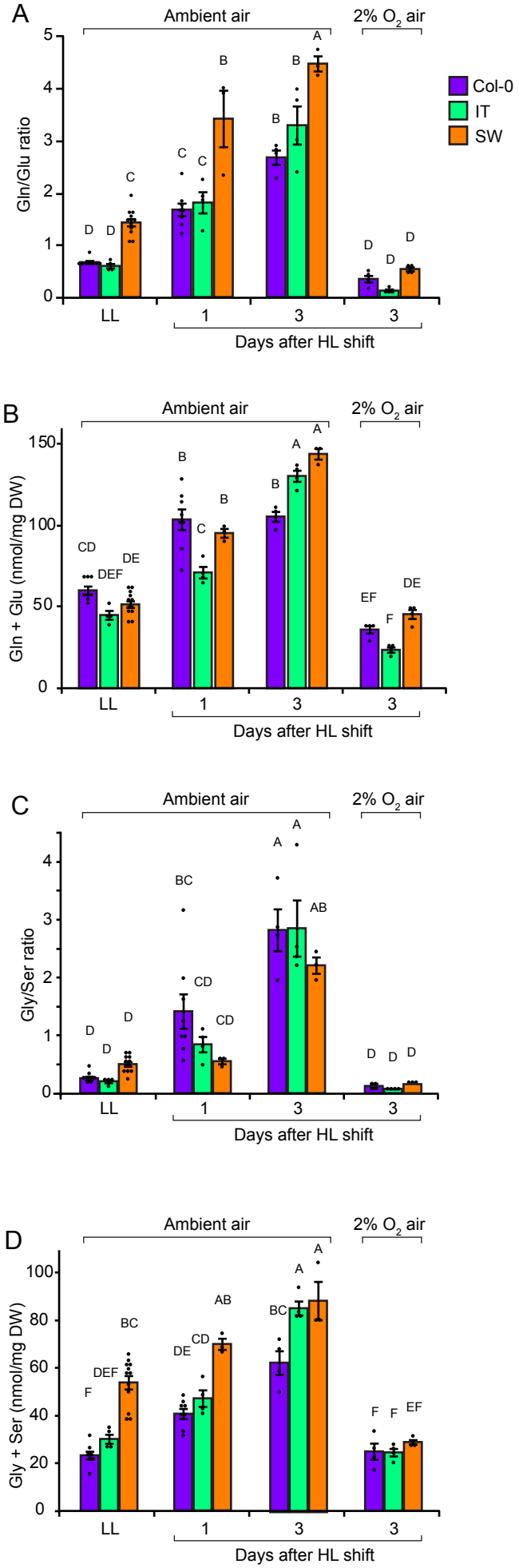
A
Ambient air
2% O2 air
Gln/Glu ratio
Col-0
IT
SW
LL
1
3
3
Days after HL shift
B
Gln + Glu (nmol/mg DW)
C
Gly/Ser ratio
D
Gly + Ser (nmol/mg DW)

Figure 7

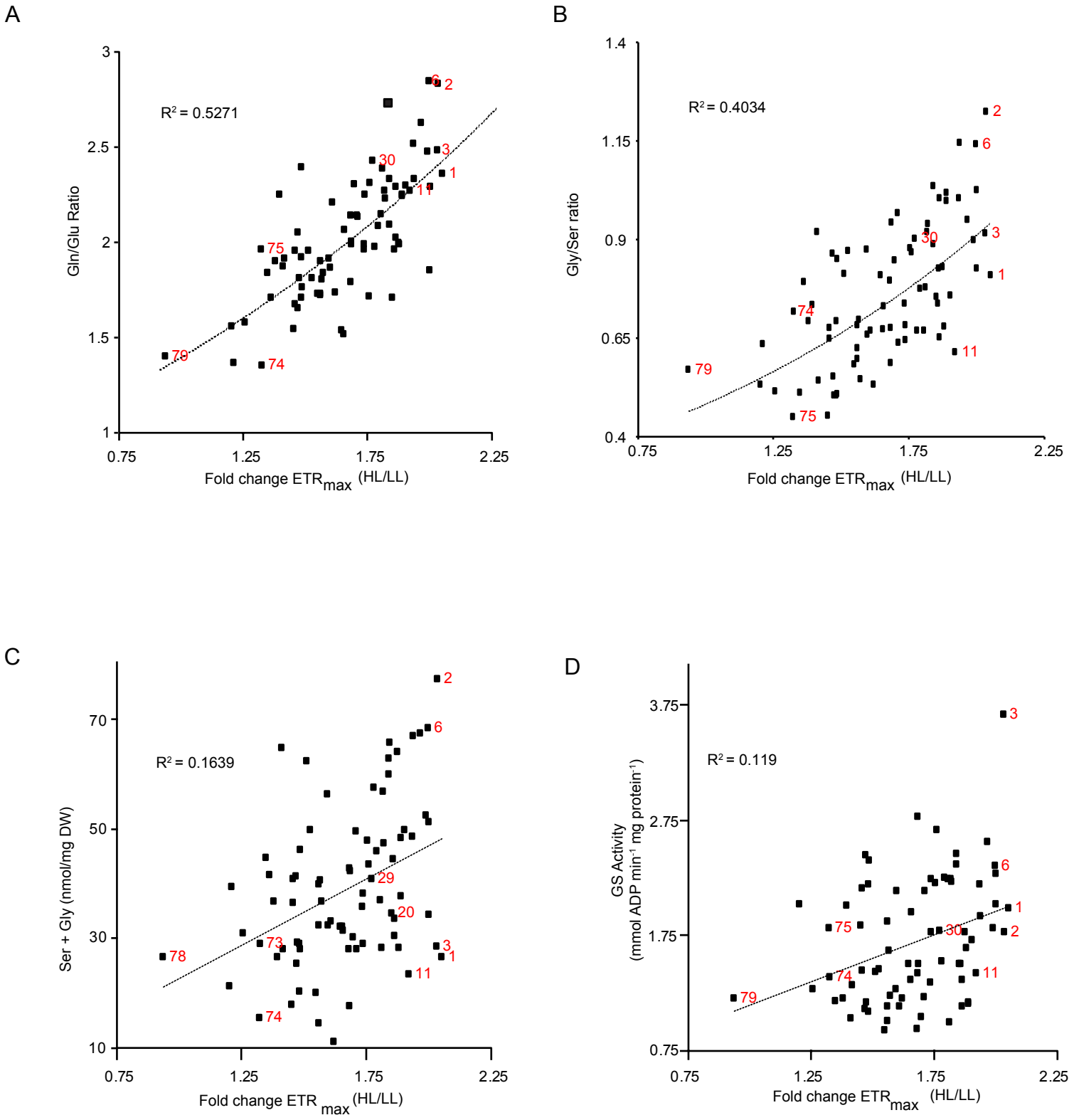
A
R² = 0.5271
Gln/Glu Ratio
Fold change ETRmax (HL/LL)
B
R² = 0.4034
Gly/Ser ratio
Fold change ETRmax (HL/LL)
C
R² = 0.1639
Ser + Gly (nmol/mg DW)
Fold change ETR max (HL/LL)
D
R² = 0.119
GS Activity
(mmol ADP min⁻¹ mg protein⁻¹)
Fold change ETRmax (HL/LL)

Figure 8

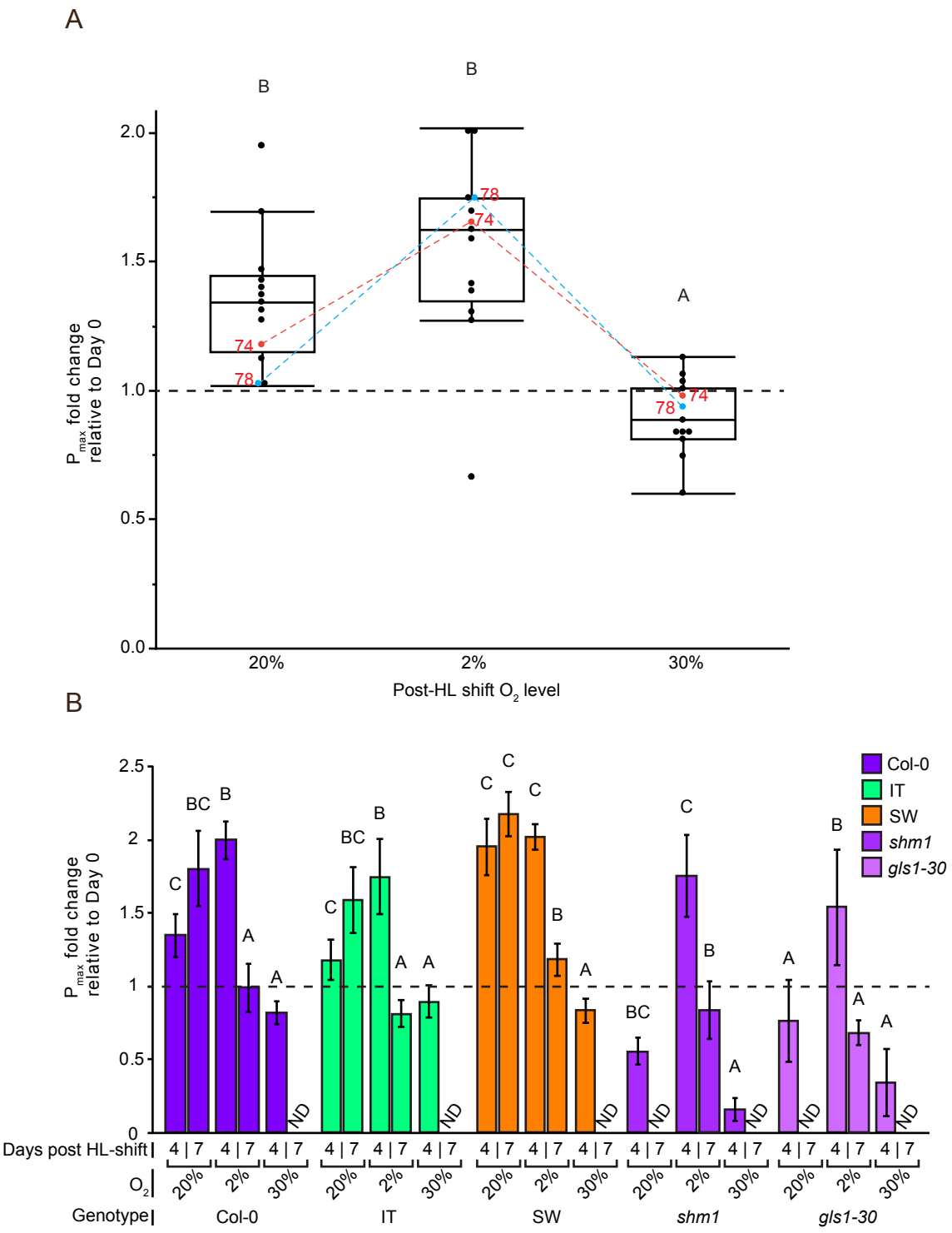
A
B
B
A
2.0
1.5
1.0
0.5
0.0
78
74
74
78
78
74
P_{max} fold change relative to Day 0
20%
2%
30%
Post-HL shift O_2 level
B
Col-0
IT
SW
shm1
gls1-30
2.5
2
1.5
1
0.5
0
P_{max} fold change relative to Day 0
C
BC
B
A
A
ND
C
BC
B
A
A
ND
C
C
C
B
A
ND
BC
ND
C
B
A
ND
A
B
A
A
ND
Days post HL-shift
4 | 7
O_2
20%
2%
30%
Genotype
Col-0
IT
SW
shm1
gls1-30

Figure 9

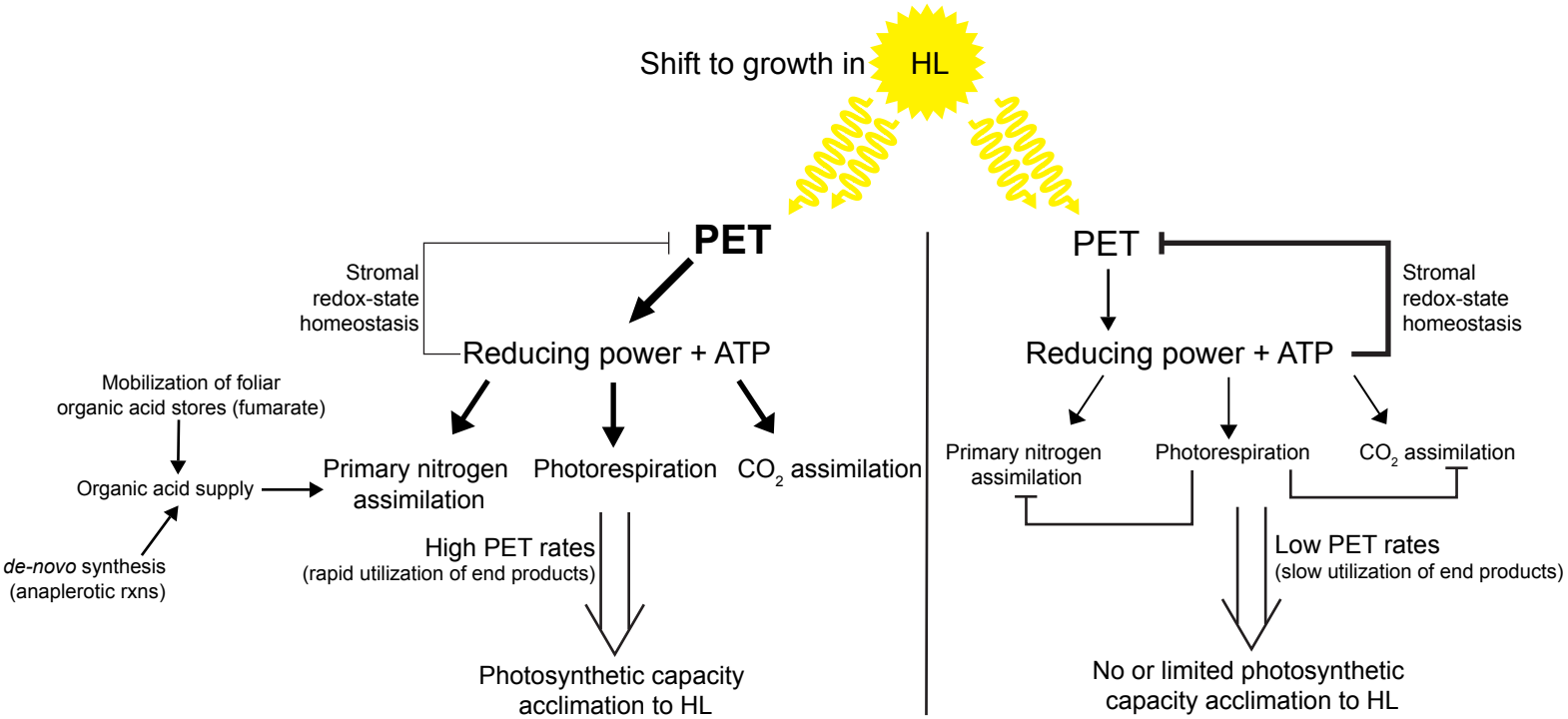
Shift to growth in
HL
PET
Stromal redox-state homeostasis
Reducing power + ATP
Mobilization of foliar organic acid stores (fumarate)
Organic acid supply
de-novo synthesis (anaplerotic rxns)
Primary nitrogen assimilation
Photorespiration
CO2 assimilation
High PET rates
(rapid utilization of end products)
Photosynthetic capacity acclimation to HL
PET
Stromal redox-state homeostasis
Reducing power + ATP
Primary nitrogen assimilation
Photorespiration
CO2 assimilation
Low PET rates
(slow utilization of end products)
No or limited photosynthetic capacity acclimation to HL

Supplemental Figure 1

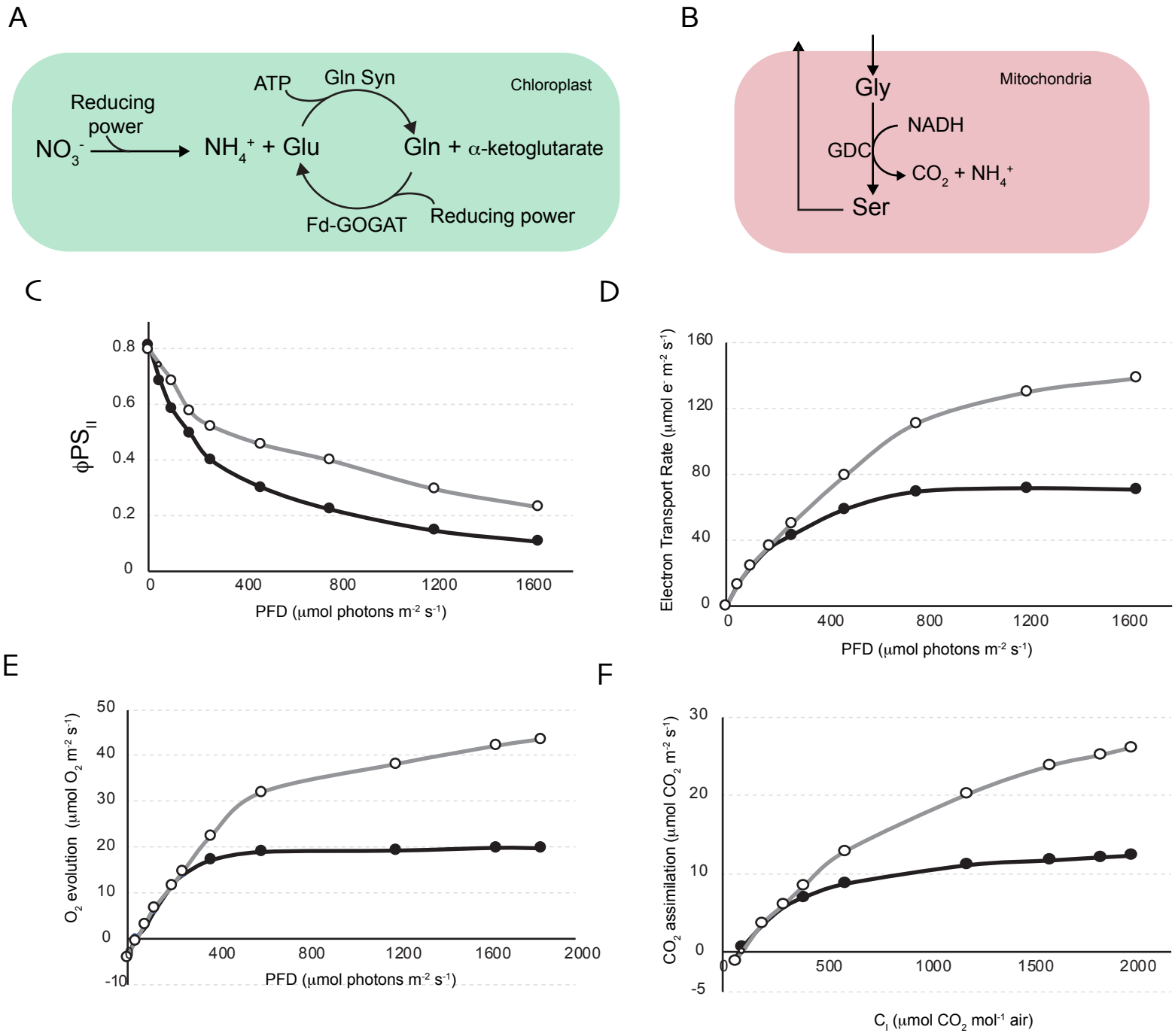

Supplemental Figure 2

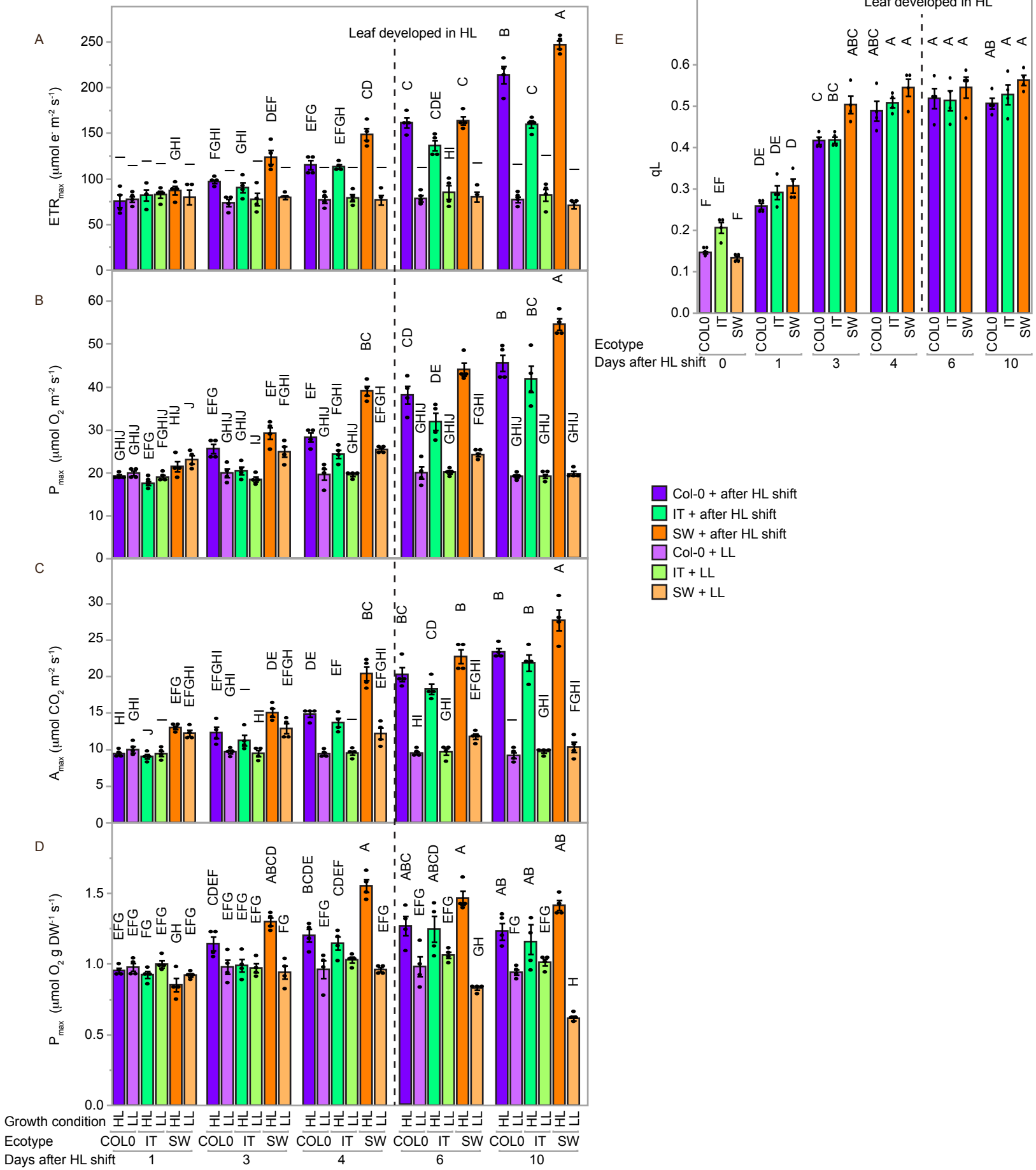

Supplemental Figure 4

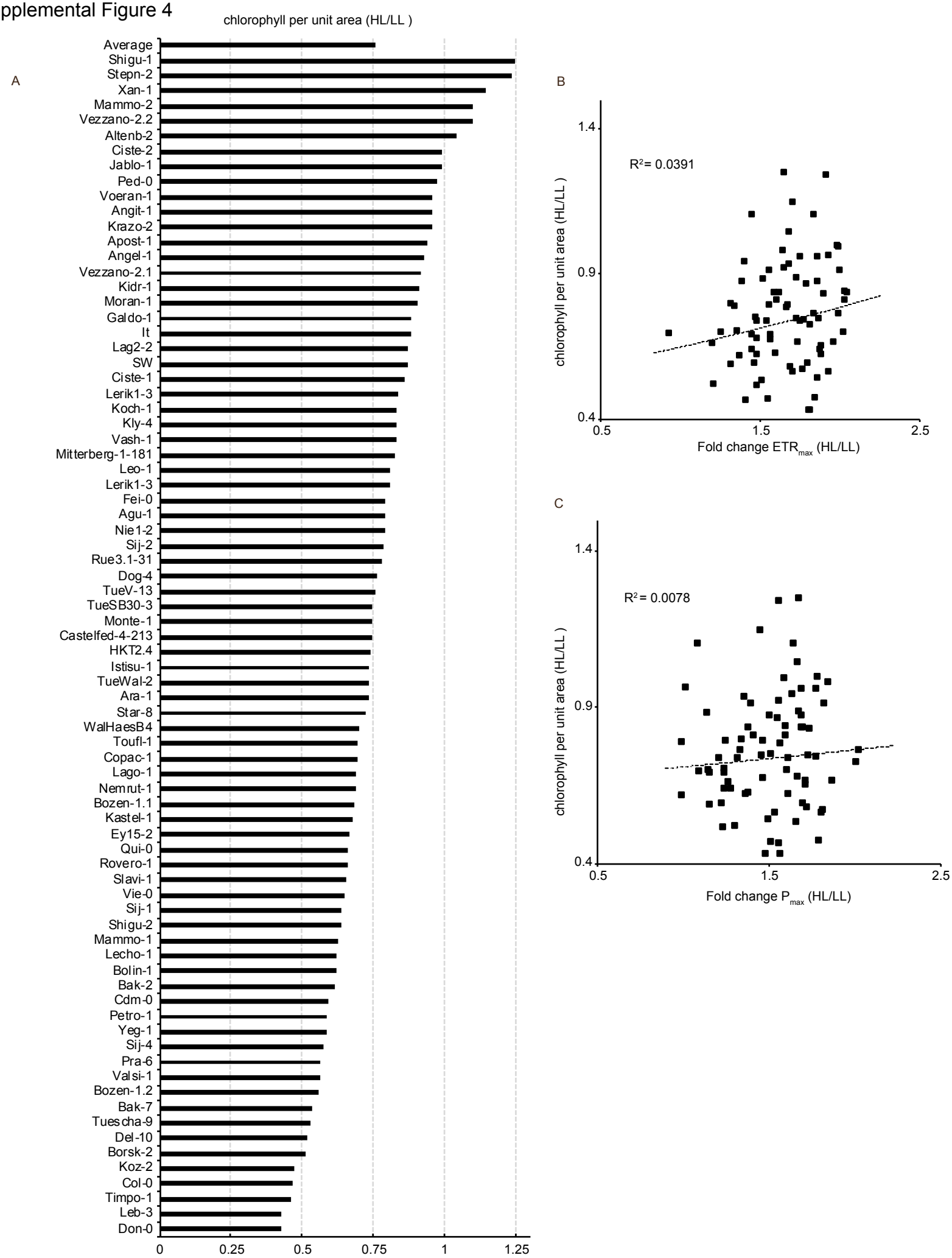

Supplemental Figure 4

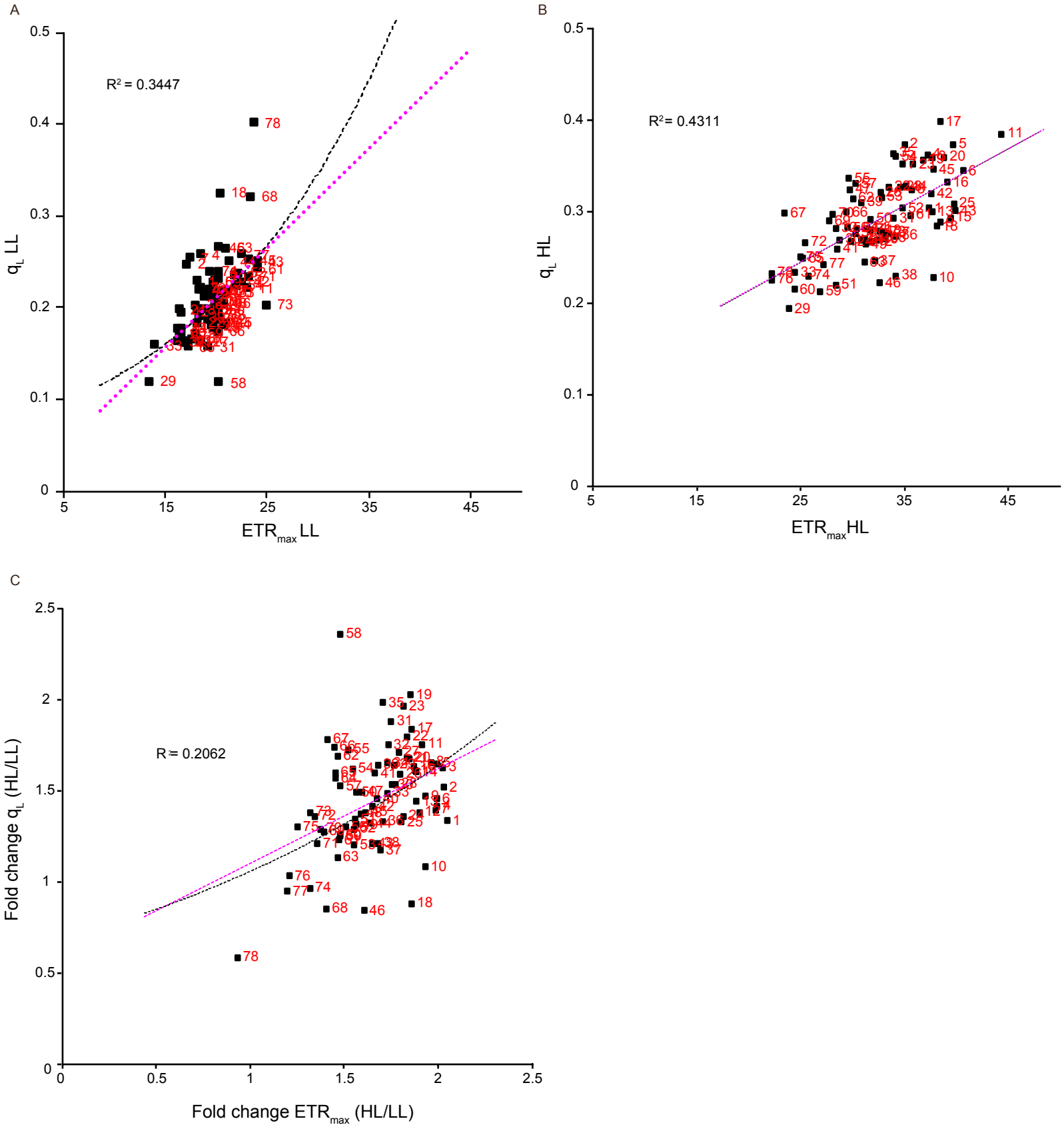

Supplemental Figure 5

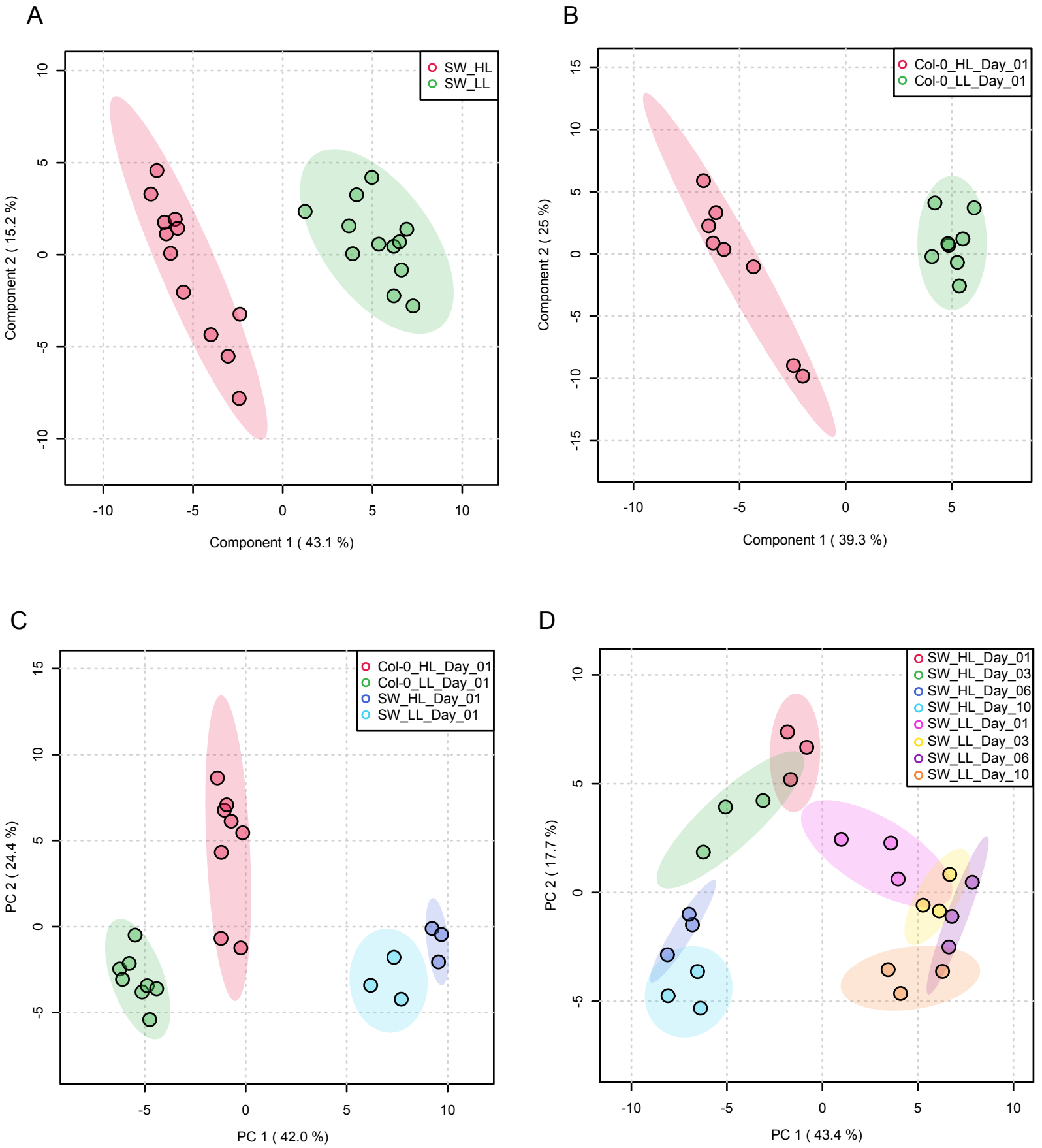

Supplemental Figure 6

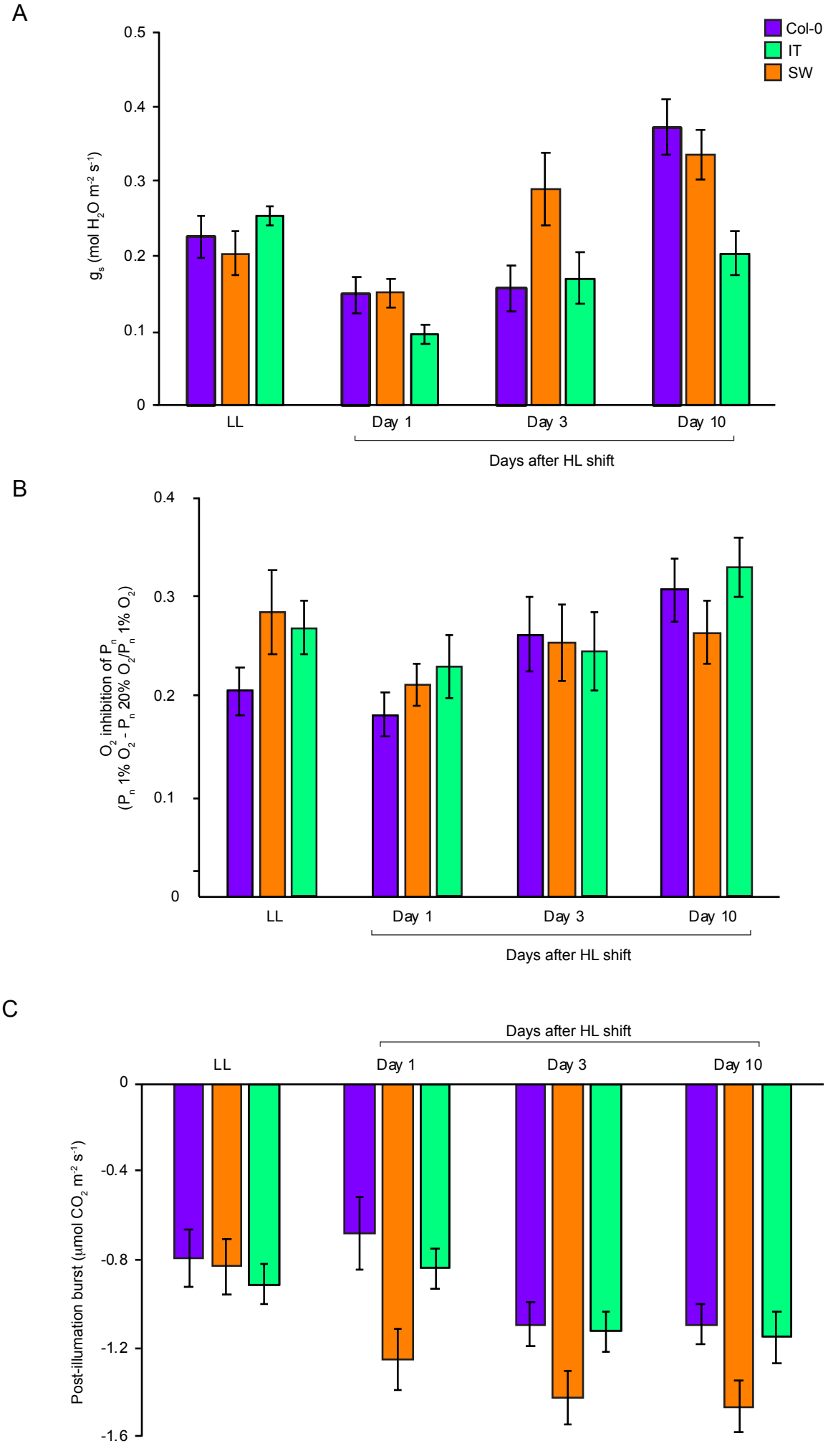

Supplemental Figure 7

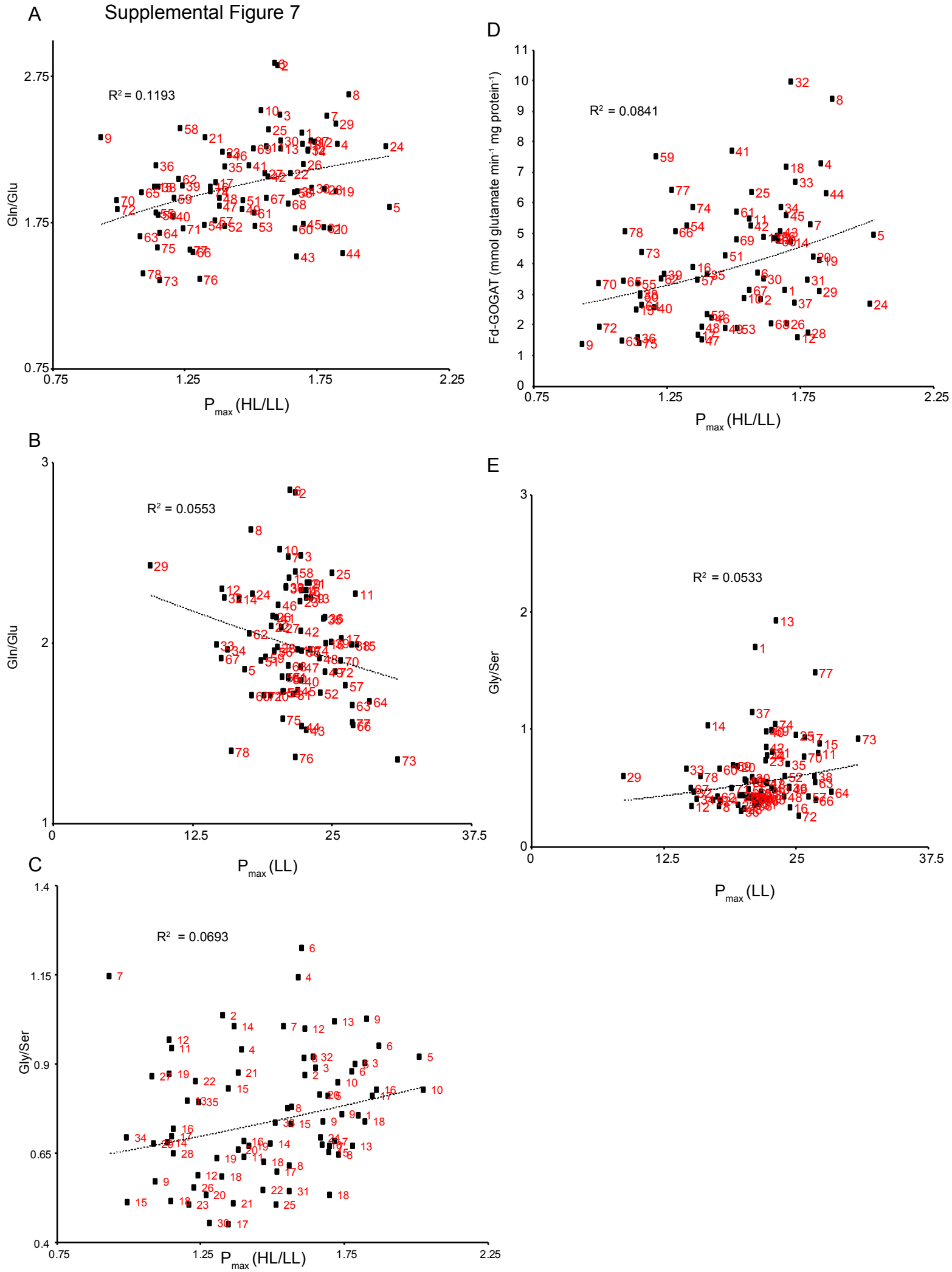

Supplemental Figure 8

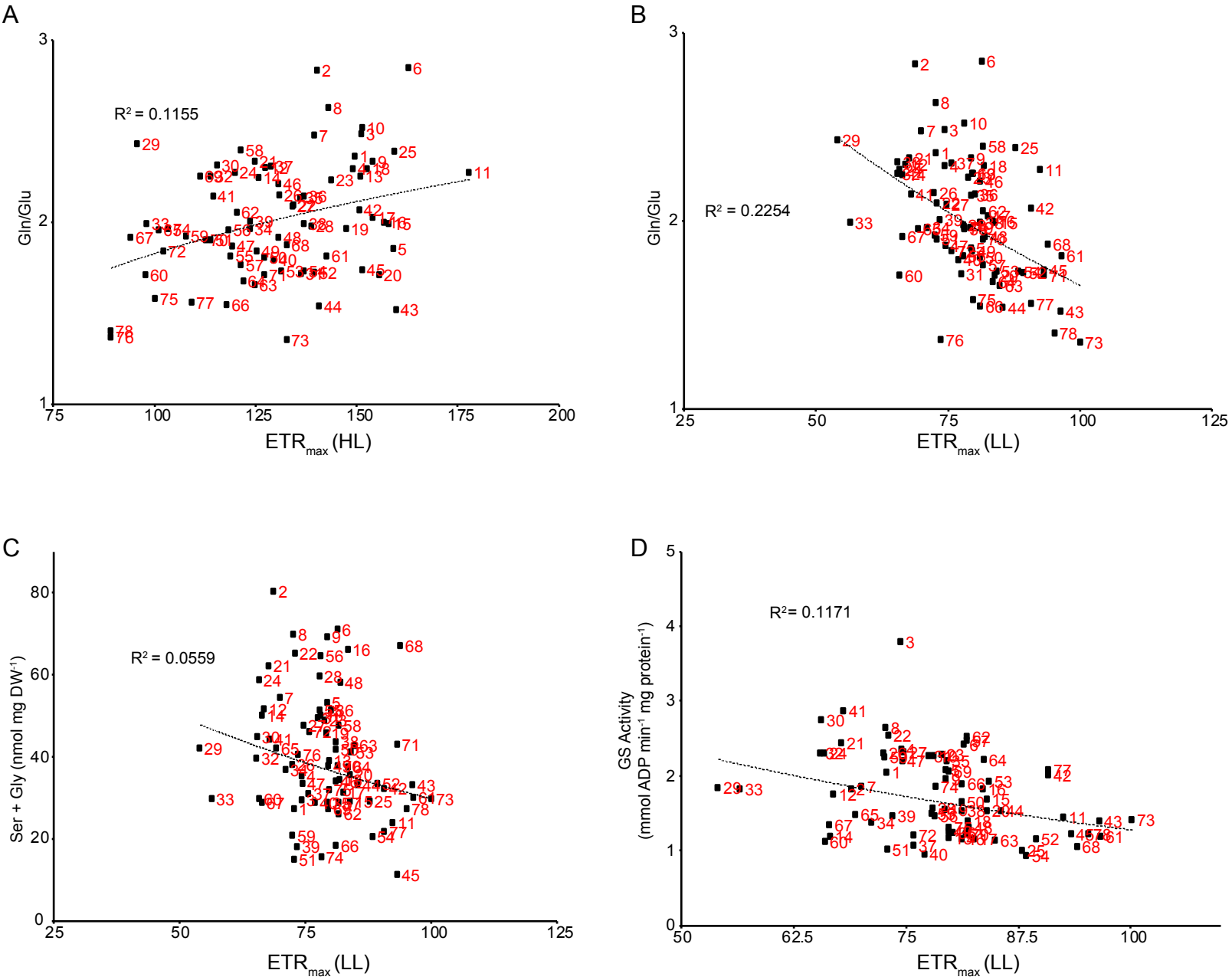
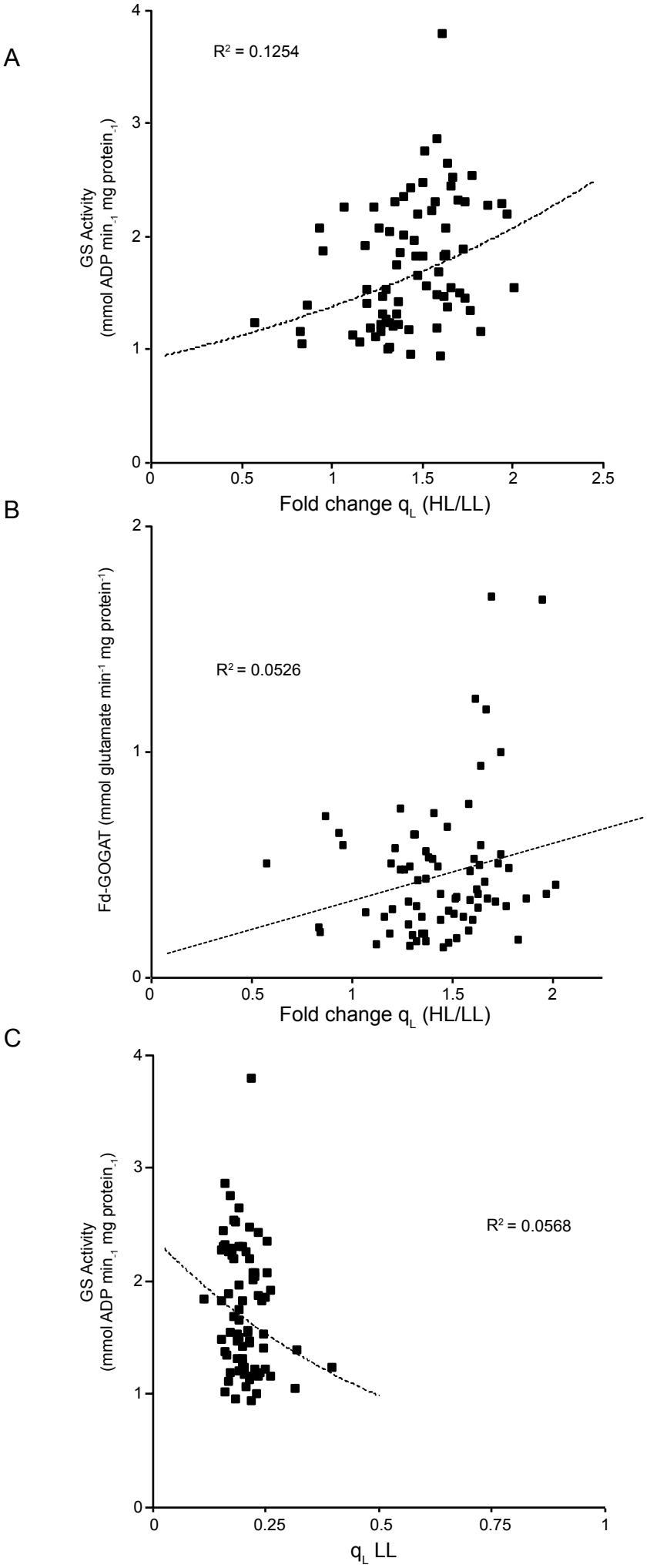
Supplemental Figure 9